Association of mitochondria with microtubules inhibits mitochondrial fission by precluding Dnm1 assembly

Kritika Mehta [a,1], Leeba Ann Chacko [a,1], Manjyot Kaur Chug [a], Siddharth Jhunjhunwala [a] and Vaishnavi Ananthanarayanan [a,2]

[a]Centre for BioSystems Science and Engineering, Indian Institute of Science, Bangalore 560012

[1] K.M. and L.A.C. contributed equally to this work

[2] Correspondence: vaishnavi@iisc.ac.in

Abstract

Mitochondria are organized as tubular networks in the cell and undergo fission and fusion. While several of the molecular players involved in mediating mitochondrial dynamics have been identified, the precise cellular cues that initiate fission or fusion remain largely unknown. In fission yeast, mitochondria are organized along microtubule bundles. Here, we employed deletions of kinesin-like proteins to perturb microtubule dynamics, and determined that cells with long microtubules exhibited long, but fewer mitochondria, whereas cells with short microtubules exhibited short, but several mitochondria due to reduced mitochondrial fission in the former and elevated fission in the latter. Correspondingly, upon onset of closed mitosis in fission yeast, wherein interphase microtubules assemble to form the spindle within the nucleus, we measured increased mitochondrial fission. We determined that the consequent rise in the mitochondrial copy number was necessary to reduce partitioning errors while stochastically partitioning mitochondria between daughter cells. We discovered that the association of mitochondria with microtubules physically impeded the assembly of the fission protein Dnm1 around mitochondria, resulting in inhibition of mitochondrial fission. Taken together, we demonstrate a novel mechanism for regulation of mitochondrial fission that is dictated by the interaction between mitochondria and the microtubule cytoskeleton.

Introduction

Mitochondria are double-membraned organelles whose functions range from ATP production to calcium signalling. Inside cells, mitochondrial form is dynamic and transitions from tubular networks to fragmented entities depending on the activity of the mitochondrial fission and fusion machinery. The major mitochondrial fission

protein is dynamin-related Drp1 GTPase (Smirnova et al., 2001) (Dnm1 in yeast (Bleazard et al., 1999; Jourdain et al., 2009)). Multimeric Drp1 rings assemble around the mitochondrial membrane and utilize the energy from GTP hydrolysis to catalyze the constriction and fission of mitochondria (Basu et al., 2017; Ingerman et al., 2005). Fusion of mitochondria requires two sets of proteins namely Opa1 (Delettre et al., 2000) for the inner membrane (Mgm1 in yeast (Sesaki et al., 2003)) and Mfn1/2 (Eura et al., 2003) for the outer membrane (Fzo1 in yeast (Hermann et al., 1998)).

The requirement for dynamic mitochondria has been attributed to two primary reasons, namely quality control and energy production (Mishra and Chan, 2016). Larger/longer mitochondria resulting from fusion are hypothesized to be capable of producing more energy whereas shorter/smaller mitochondria formed following a fission event are likely to undergo mitophagy (Chen and Chan, 2009). In the case of the latter, fission could serve as an efficient mechanism to segregate and eliminate damaged mitochondria. Dysfunction of fission and fusion processes has been implicated in neurodegeneration (Deng et al., 2008; Hirai et al., 2001), cancer (Graves et al., 2012) and cardiomyopathies (Ashrafian et al., 2010), amongst a host of metabolic disorders.

In mammalian cells, mitochondria are transported along microtubule tracks by the activity of motor proteins kinesin-1 and dynein (Pilling et al., 2006). Kinesin-1 and dynein bind to the outer membrane of mitochondria via the Miro/Milton complex (Glater et al., 2006; Stowers et al., 2002; van Spronsen et al., 2013) and move mitochondria in the anterograde and retrograde direction respectively. In neuronal cells, increase in calcium levels results in the attachment of kinesin-1 motor to mitochondria via syntaphilin, which inhibits the ATPase activity of kinesin and hence

leads to stationary mitochondria on neuronal microtubules (Chen and Sheng, 2013). About 70% of mitochondria in neuronal cells have been visualized in this stationary state (Kang et al., 2008). In contrast to mammalian cells, mitochondria in fission yeast do not undergo motor-driven movement along microtubules (Chiron et al., 2008; Yaffe et al., 2003). However, the protein Mmb1 has been identified to associate mitochondria with dynamic microtubules (Fu et al., 2011). Upon microtubule depolymerization using methyl benzimidazol-2-yl-carbamate (MBC), mitochondria have been observed to undergo fragmentation (Fu et al., 2011; Jourdain et al., 2009; Li et al., 2015). Additionally, mitochondrial dynamics and partitioning in fission yeast have been observed to be actin/myosin-independent processes (Jourdain et al., 2009), contrary to the mechanism of mitochondrial partitioning in budding yeast (Fehrenbacher et al., 2004).

Cells employ several strategies to reduce partitioning error of organelles during mitosis, such as ordered segregation mediated by spindle poles, or increasing copy numbers of organelles prior to cell division (Huh and Paulsson, 2011). In the latter, homogeneous distribution of the multiple organelle copies serves to increase the probability of equal partitioning stochastically. Mitochondrial inheritance has been observed to be microtubule-dependent in mammalian cells (Lawrence and Mandato, 2013). In fission yeast, mitochondrial partitioning during cell division has been proposed to be mediated by attachment of mitochondria with spindle poles (Jajoo et al., 2016; Krüger and Tolic, 2008; Yaffe et al., 2003), similar to the segregation of endosomes, lysosomes and Golgi bodies in mammalian cells (Bergeland et al., 2001; Shima et al., 1998) . However, only a portion of the observed mitochondria associated with the spindle poles (Yaffe et al., 2003). Additionally, increased mitochondrial fragmentation upon the onset of mitosis has also been

observed (Jourdain et al., 2009), perhaps indicating a stochastic mechanism for mitochondrial partitioning.

While the molecular players that effect fission and fusion have been identified in several systems, the cellular signals that regulate these events are largely elusive. Here, we demonstrate that mitochondria piggyback on dynamic microtubules to selectively undergo fission when microtubules depolymerize. Reorganization of interphase microtubules into the nucleus when cells prepare for division also provided the cue for increased mitochondrial fission. We quantified the number of mitochondria in mother cells immediately after formation of mitotic spindle within the nucleus and the number of mitochondria in the resulting daughter cells, and confirmed that the partitioning was indeed a good fit to a binomial distribution, indicating that the mitochondria were stochastically segregated into the two daughter cells. We determined that the presence of long and stabilized microtubules was inhibitory to unopposed fission even when Dnm1 was overexpressed. Finally, we discovered microtubule-bound mitochondria were unlikely to undergo fission due to the unavailability of space between microtubules and mitochondria for the formation of the Dnm1 ring.

Materials and Methods

Strains and media. The fission yeast strains used in this study are listed in Table S1. All the strains were grown in YE (yeast extract) media or Edinburg Minimal media (EMM) (Forsburg and Rhind, 2006) with appropriate supplements at a temperature of 30˚C. Cells that were transformed with plasmid pREP41-Dnm1 or pREP41-Dnm1-Cterm-GFP (see Table S1) were cultured in EMM with appropriate supplements and 0.05μM thiamine for partial induction of the nmt1 promoter. Strains VA076 and VA084 were constructed by crossing PT2244 with FY20823, and Dnm1Δ with G5B respectively (see Table S1), following the random spore analysis protocol (Forsburg and Rhind, 2006).

Plasmid transformation. Transformation of strains was carried out using the improved protocol for rapid transformation of fission yeast (Kanter-Smoler et al., 1994). In brief, cells were grown overnight to log phase in low glucose EMM, pelleted and washed with distilled water. The cells were then washed in a solution of lithium acetate/EDTA (100mM LiAc, 1mM EDTA, pH 4.9) and re-suspended in the same solution. 1μg of plasmid DNA was added to the suspension, followed by addition of lithium acetate/PEG (40% w/v PEG, 100mM LiAc, 1mM EDTA, pH 4.9) and then incubated at 30°C for 30 min in a shaking incubator. This was followed by a heat shock of 15min at 42°C. Thereafter, cells were pelleted down, re-suspended in TE solution (10mM Tris-HCl, 1mM EDTA, pH 7.5) and plated onto selective EMM plates.

Preparation of yeast for imaging. For imaging mitochondria, fission yeast cells were grown overnight in a shaking incubator at 30°C, washed once with distilled water, and stained with 200nM Mitotracker Orange CMTMRos (ThermoFisher Scientific, Cat. #M7510) dissolved in EMM for 20min. Following this, cells were washed thrice with EMM and then allowed to adhere on lectin-coated (Sigma-

119 Aldrich, St. Louis, MO, Cat. #L2380) 35mm confocal dishes (SPL, Cat. #100350) for
120 20min. Unattached cells were then removed by washing with EMM. In experiments
121 where mitochondria were not imaged, staining with Mitotracker was omitted.
122 **Microtubule depolymerization.** For depolymerization of microtubules, cells were
123 treated with methyl benzimidazol-2-yl-carbamate (MBC, Carbendazim 97%, Sigma
124 Aldrich). A stock solution with a concentration of 25mg/ml was prepared in DMSO
125 and later diluted to a working concentration of 25µg/ml in EMM.
126 **Microscopy.** Confocal microscopy was carried out using the InCell Analyzer-6000
127 (GE Healthcare, Buckinghamshire, UK) with 60x/0.7 N.A. objective fitted with an
128 sCMOS 5.5MP camera having an x-y pixel separation of 108nm. For GFP and
129 Mitotracker Orange imaging, 488 and 561nm laser lines and bandpass emission
130 filters 525/20 and 605/52nm respectively were employed. Time-lapses for
131 visualization of mitochondrial dynamics were captured by obtaining 5 Z-stacks with a
132 0.5µm-step size every 12s. Deconvolution was performed in images obtained using
133 a Deltavision RT microscope (Applied Precision) with a 100×, oil-immersion 1.4 N.A.
134 objective (Olympus, Japan). Excitation of fluorophores was achieved using
135 InsightSSI (Applied Precision) and corresponding filter selection for excitation and
136 emission of GFP and Mitotracker Orange. Z-stacks with 0.3µm-step sizes
137 encompassing the entire cell were captured using a CoolSnapHQ camera
138 (Photometrics), with 2X2 binning. The system was controlled using softWoRx 3.5.1
139 software (Applied Precision) and the deconvolved images obtained using the built-in
140 setting for each channel.
141 **3D visualization of deconvolved images**. 3D views of the microtubules and
142 mitochondria in Movies S2, S3, S4, S8, S9, S10, S12 and S13 were obtained from
143 deconvolved images captured in the Deltavision microscope using Fiji's '3D project'

144 function, with the brightest point projection method and 360˚ total rotation with 10˚
145 rotation angle increment.
146 **Estimation of volume of mitochondria.** Mitochondrial volume was estimated in Fiji
147 by integrating the areas of mitochondria in thresholded 3D stacks of cells in
148 fluorescent deconvolved images obtained using the Deltavision RT microscope. The
149 total volume was then normalized to the mean total mitochondrial volume of wild-
150 type cells. Individual mitochondrial volumes were estimated in the same fashion.
151 **Analysis of mitochondrial dynamics.** Individual mitochondria were identified in
152 each frame of the time-lapse obtained in confocal mode of the GE InCell Analyzer
153 after projecting the maximum intensity of the 3D stack encompassing the cell,
154 followed by mean filtering and visualization in Fiji's 'mpl-magma' lookup table.
155 Following identification of mitochondria, the 'Measure' function of Fiji was employed
156 to obtain the circularity, aspect ratio and parameters of fitted ellipse. The length of
157 the major axis of the ellipse fitted to a mitochondrion was defined as the size of that
158 mitochondrion. The size, circularity and aspect ratio were estimated for mitochondria
159 at each frame and each time point. Fission and fusion frequencies of mitochondria
160 were estimated by counting the number of mitochondria identified during each frame
161 of the time-lapse. The difference in number of mitochondria from one frame to the
162 next was counted, with an increase being counted as fission event and decrease as
163 fusion event. The total number of fission events and fusion events per cell were
164 estimated and divided by the total duration of the time-lapse to obtain the fission and
165 fusion frequencies.
166 **Test for fit of mitochondrial partitioning during mitosis to binomial**
167 **distribution.** To test the fit of mitochondrial segregation during mitosis to a binomial
168 distribution, the data were z-transformed as previously described (Hennis and Birky,

1984). Briefly, given n mitochondria in the mother cell just prior to cell division, x and $n - x$ mitochondria in the resulting daughter cells, z was given by $2x - n/\sqrt{n}$ to approximate the binomial distribution to a normal distribution of 0,1. The z values obtained for each x and n were binned into k bins of equal sizes and subjected to Chi-square test with $k - 1$ degrees of freedom. The z values are expected to be equally distributed among the k bins, with expected number of $1/k$ per bin.

Data analysis and plotting. Data analysis was performed in Matlab (Mathworks, Natick, MA). Box plots with the central line indicating the median and notches that represent the 95% confidence interval of the median were obtained by performing one-way ANOVA ('anova1' in Matlab) or Kruskal-Wallis Test ('kruskalwallis' in Matlab). The former was used when data were found to be normally distributed and the latter when data were non-normally distributed (tested using 'chi2gof' in Matlab). Following this, significant difference ($p<0.05$) was tested using the Tukey's Honestly Significant Difference procedure ('multcompare' in Matlab). All the plots were generated using Matlab.

185 **Results**

186 **1. Perturbation of microtubule dynamics leads to changes in mitochondrial**

187 **numbers**

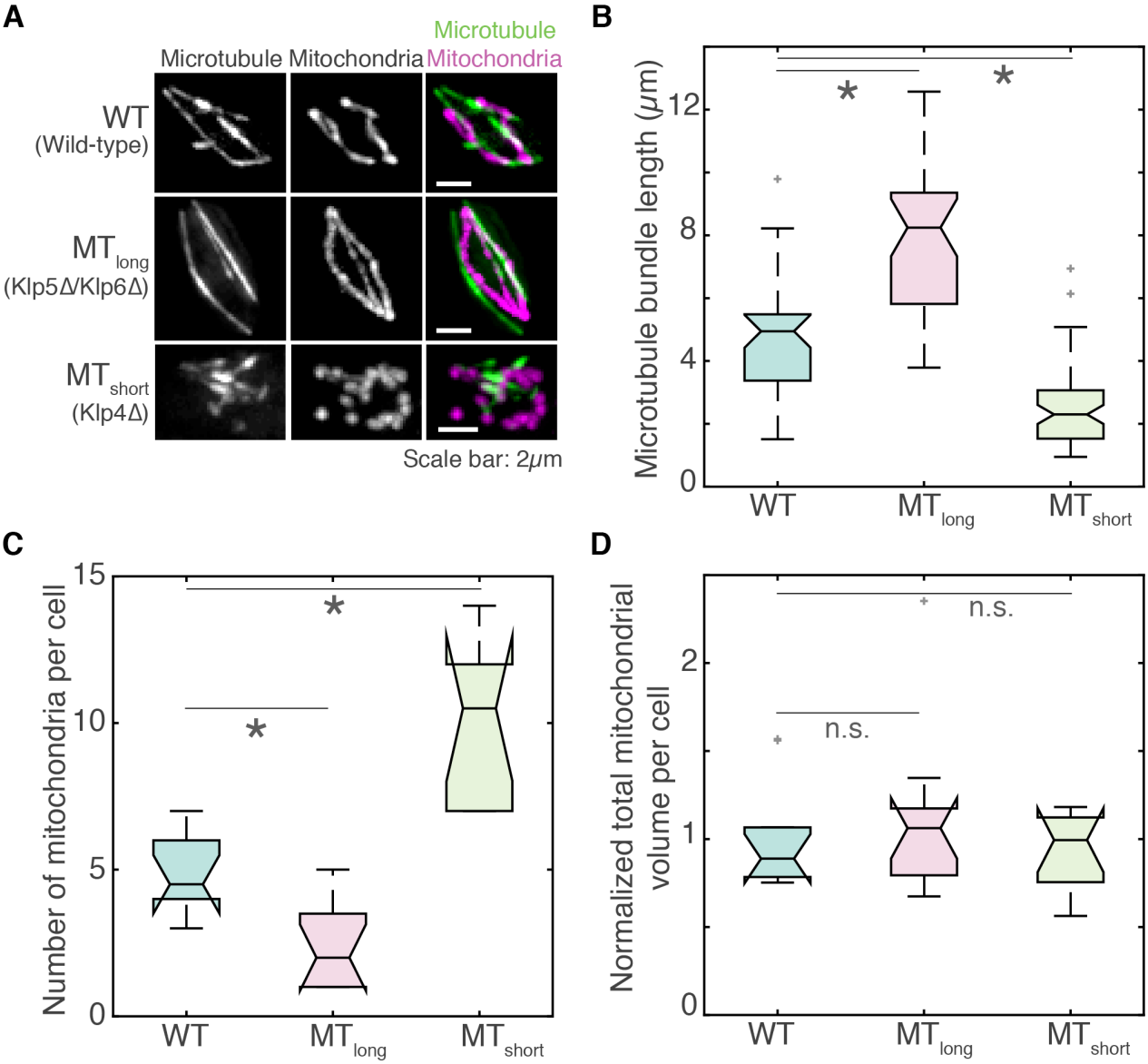

Figure 1. Mitochondrial number is inversely proportional to microtubule length. **(A)** Maximum intensity projections of deconvolved Z-stack images of microtubules (left), mitochondria (centre) and their composite (right) in wild-type ('WT', top, strain KI001, see Table S1), Klp5Δ/Klp6Δ ('MT_{long}', strain G3B, see Table S1) and Klp4Δ ('MT_{short}', strain G5B, see Table S1) cells. **(B)** Box plot of length of anti-parallel microtubule bundles in WT, MT_{long} and MT_{short} cells (n=40, 37 and 63 bundles respectively). **(C)** Box plot of number of mitochondria per cell in WT, MT_{long}

and MT_{short} cells (*n*=10, 12 and 13 cells respectively). **(D)** Box plot of the total volume of mitochondria per cell in WT, MT_{long} and MT_{short} cells normalized to mean total wild-type mitochondrial volume (*n*=10, 12 and 13 cells respectively). In B-D, light grey crosses represent outliers, asterisk represents significance ($p<0.05$) and 'n.s.' indicates no significant difference (one-way ANOVA, Tukey's Honestly Significant Difference procedure).

188 We observed that mitochondria underwent increased fission upon microtubule
189 depolymerization, but did not observe their subsequent aggregation as reported
190 previously (Fig. S1A-C). Instead, the fragmented mitochondria were mobile and
191 frequently in close contact with each other (Fig. S1B, C, Movie S1). Since the
192 depolymerization of microtubules had a direct effect on mitochondrial fission, we set
193 out to study the consequence of modification of microtubule dynamics on
194 mitochondrial dynamics. To this end, we visualised the mitochondria and
195 microtubules of fission yeast strains carrying deletions of antagonistic kinesin-like
196 proteins, Klp5/Klp6 and Klp4 in high-resolution deconvolved images (Fig. 1A, Movies
197 S2, S3 and S4).

198 The heteromeric Klp5/Klp6 motor is required for maintenance of interphase
199 microtubule length by promoting catastrophe at microtubule plus ends (Tischer et al.,
200 2009; West et al., 2001). Cells lacking Klp5 and Klp6 exhibited long microtubule
201 bundles ('MT_{long}', Fig. 1B) as reported previously due to a decreased catastrophe
202 rate (Tischer et al., 2009). In contrast, Klp4 is required for polarized growth in fission
203 yeast and has been suggested to promote microtubule growth (Browning et al.,
204 2000; Busch et al., 2004). As a result, in the absence of Klp4, microtubule bundles
205 were only about half the length of wild-type bundles ('MT_{short}', Fig. 1B).

206 As in wild-type cells, mitochondria in Klp5Δ/Klp6Δ were in close contact with
207 the microtubule, whereas we observed reduced association between the short

208 microtubules and mitochondria in Klp4Δ cells (Fig. 1A, Movies S3 and S4). While
209 wild-type cells had 4.9 ± 0.4 (mean ± s.e.m.) mitochondria per cell, we observed that
210 Klp5Δ/Klp6Δ contained only 2.3 ± 0.4 (mean ± s.e.m.). In contrast, Klp4Δ cells had
211 10 ± 0.9 mitochondria per cell (mean ± s.e.m., Fig. 1C). This indicated that the
212 number of mitochondria per cell was inversely related to the length of microtubule
213 bundle. However, the decrease in the number of mitochondria in Klp5Δ/Klp6Δ cells
214 and increase in Klp4Δ cells were not at the expense of mitochondrial volume, since
215 the net mitochondrial volume in both cases was comparable to wild-type
216 mitochondrial volume (Fig. 1D), with individual mitochondrial volumes changing to
217 compensate for the difference in mitochondrial numbers between WT, Klp5Δ/Klp6Δ
218 and Klp4Δ cells (Fig. S1D).

219 **2. Cells with short microtubules undergo increased fission**

220 To understand the difference in mitochondrial numbers in wild-type,
221 Klp5Δ/Klp6Δ and Klp4Δ cells, we acquired and analyzed time-lapse videos at the
222 single mitochondrion level in all three cases (Fig. 2A, Movies S5, S6 and S7). Similar
223 to our observations from high-resolution images, we measured 3.6 ± 0.2, 2.7 ± 0.2,
224 and 6.9 ± 0.8 mitochondria (mean ± s.e.m.) in wild-type, Klp5Δ/Klp6Δ and Klp4Δ
225 cells respectively (Fig. 1C and 2B). Analysis of evolution of these mitochondrial
226 numbers revealed no significant changes over time (Fig. 2B). Additionally,
227 mitochondria in wild-type cells underwent ~1 fission and ~1 fusion event every
228 minute on an average, whereas Klp5Δ/Klp6Δ cells exhibited a fission frequency that
229 was half that of wild-type, and Klp4Δ mitochondria had a fission frequency that was
230 almost double that of wild-type (Fig. 2C). The fusion frequency of mitochondria in
231 Klp4Δ cells was slightly higher than in wild-type and Klp5Δ/Klp6Δ cells (Fig. 2D),
232 likely due to the increased number of mitochondria in Klp4Δ cells that could

233 participate in fusion. However, the resulting ratio of the mean fission frequency to the
234 mean fusion frequency was ~1, ~0.5 and ~1.3 in wild-type, Klp5Δ/Klp6Δ and Klp4Δ
235 cells respectively. We therefore concluded that the difference in mitochondrial
236 numbers between wild-type cells and Klp5Δ/Klp6Δ and Klp4Δ arose primarily due to
237 the changes in fission frequencies of mitochondria.

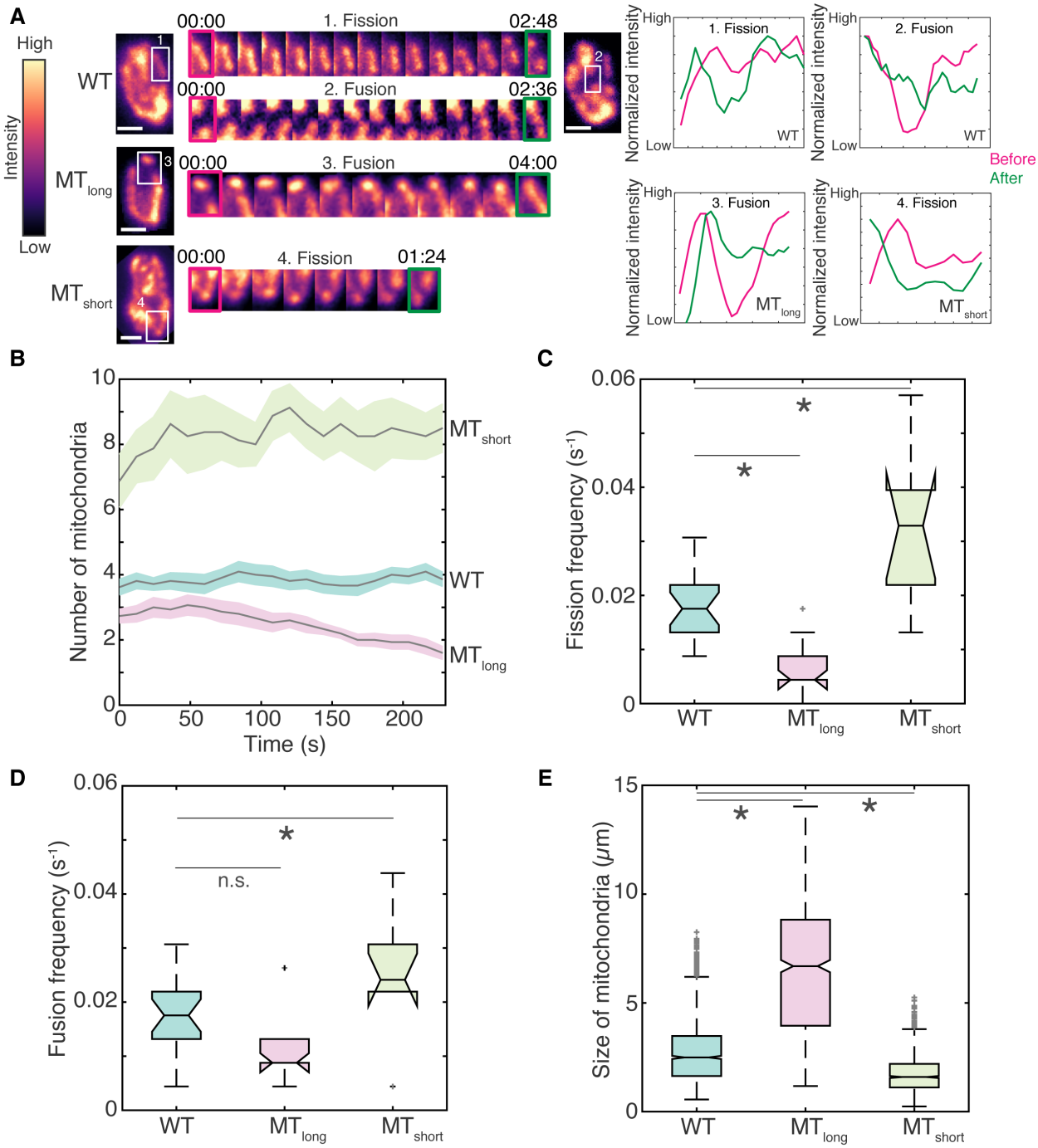

Figure 2. Microtubule length determines fission frequency of mitochondria. (A) Montage of maximum intensity projected confocal Z-stack images of wild-type ('WT', strain KI001, see Table S1), Klp5Δ/Klp6Δ ('MT_{long}', strain G3B, see Table S1) and Klp4Δ ('MT_{short}', strain G5B, see Table S1) cells represented in the intensity map indicated to the left of the images. The insets (white box) and their montages on the right of the images are representative fission and fusion events in WT ('1' and '2'), fusion event in MT_{long} ('3') and fission event in MT_{short} cell ('4'). Time is indicated as 'mm:ss' above the montage of the insets. The normalized intensity along the mitochondrion in the inset before (magenta) and after (green) the fission or fusion event is indicated in plots to the right of the montages. **(B)** Evolution of mitochondrial number over time indicated as mean (solid grey line) and standard error of the mean (shaded region) for WT, MT_{long} and MT_{short} cells (*n*=21, 15 and 8 cells respectively. **(C)** Box plot of the fission frequency of mitochondria per second in WT, MT_{long} and MT_{short} cells (*n*=21, 15 and 8 cells respectively). **(D)** Box plot of the fusion frequency of mitochondria per second in WT, MT_{long} and MT_{short} cells (*n*=21, 15 and 8 cells respectively). **(E)** Box plot of the size of mitochondria in WT, MT_{long} and MT_{short} cells, calculated as the length of the major axis of an ellipse fitted to each mitochondrion (*n*=1613, 739 and 1326 mitochondria respectively). In C-E, light grey crosses represent outliers, asterisk represents significance ($p<0.05$) and 'n.s.' indicates no significant difference (one-way ANOVA in C and D, Kruskal-Wallis test in E, Tukey's Honestly Significant Difference procedure).

Note that the rate of mitochondrial fission (per second per mitochondrion) was comparable to the rate of mitochondrial fusion (per second per mitochondrion) in all three cases, resulting in the constant number of mitochondria we measured over time (Fig. 2B). As observed in the high resolution deconvolved images, we also measured significant differences in the size and morphology of the mitochondria in WT, Klp5Δ/Klp6Δ and Klp4Δ cells (Fig. 2E, Fig. S2). Mitochondrial sizes reflected microtubule bundle lengths, with the largest mitochondria in Klp5Δ/Klp6Δ cells and the smallest in Klp4Δ cells. WT cells predictably had mitochondrial sizes between that of Klp4Δ and Klp5Δ/Klp6Δ cells (Fig. 2E, Fig. S2).

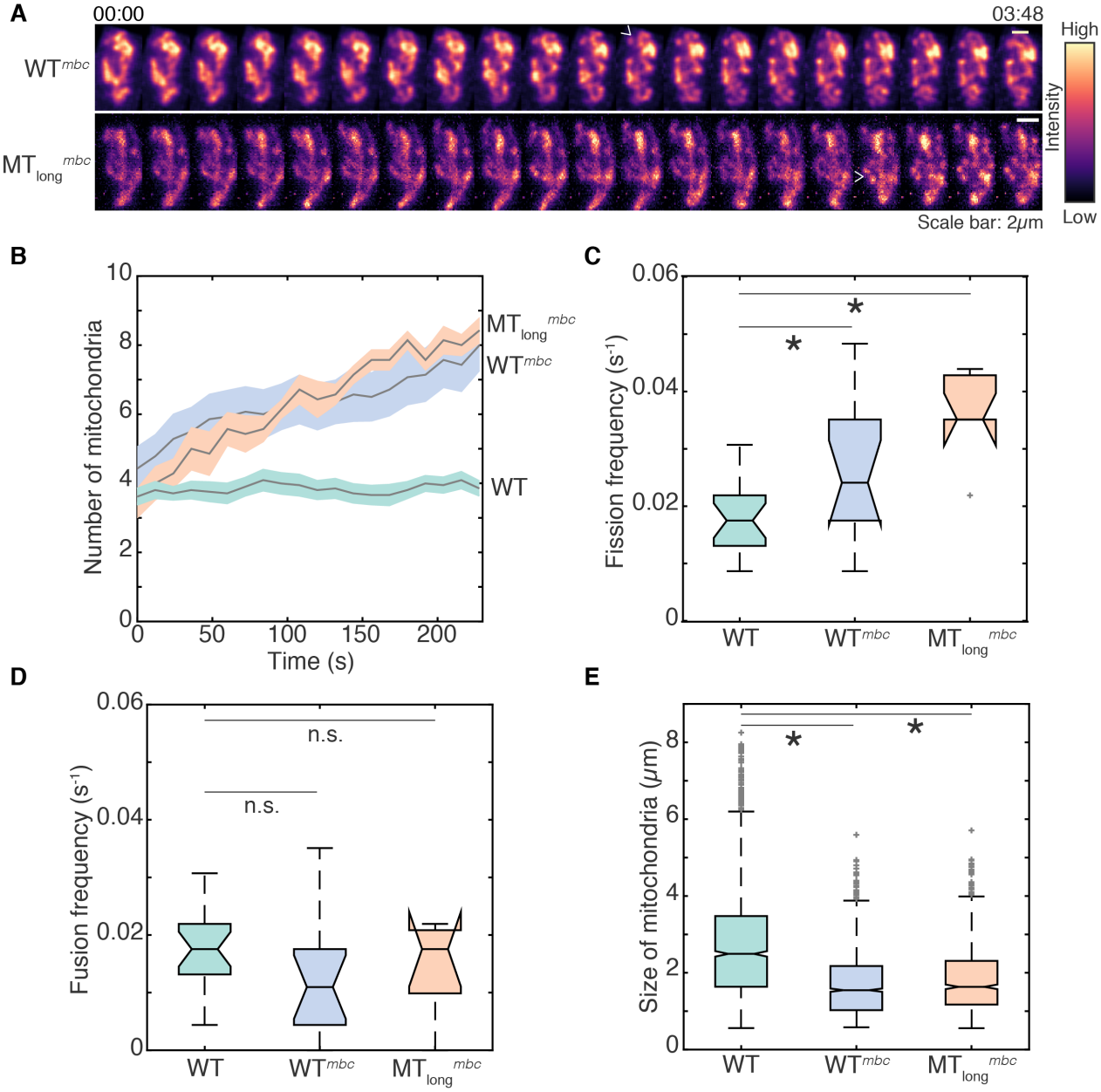

Figure 3. Microtubule depolymerization induces increased fission in WT and Klp5Δ/Klp6Δ cells. (A) Montage of maximum intensity projected confocal Z-stack images of MBC-treated wild-type (WT^{mbc}, strain KI001, see Table S1) and Klp5Δ/Klp6Δ ('MT_{long}^{mbc}', strain G3B, see Table S1) cells represented in the intensity map indicated to the right of the images. White open arrowheads point to representative fission events. 00:00 indicates time (mm:ss) 2min after addition of MBC. **(B)** Evolution of mitochondrial number with time indicated as mean (solid grey line) and standard error of the mean (shaded region) for wild-type ('WT'), WT^{mbc}, and MT_{long}^{mbc} cells (*n*=21, 14 and 7 cells respectively). **(C)** Box plot of the fission frequency of mitochondria per second in WT, WT^{mbc}, and MT_{long}^{mbc} cells (*n*=21, 14

and 7 cells respectively). **(D)** Box plot of the fusi frequency of mitochondria per second in WT, WT^{mbc}, and MT_{long}^{mbc} cells (*n*=21, 14 and 7 cells respectively). **(E)** Box plot of the size of mitochondria in WT, WT^{mbc}, and MT_{long}^{mbc} cells, calculated as the length of the major axis of an ellipse fitted to each mitochondrion (*n*=1613, 1765 and 886 mitochondria respectively). In C-E, light grey crosses represent outliers, asterisk represents significance ($p<0.05$) and 'n.s.' indicates no significant difference (one-way ANOVA in C and D, Kruskal-Wallis Test in E, Tukey's Honestly Significant Difference procedure). Note that the WT data represented in this figure is the identical to the wild-type data plotted in Fig. 2 and Fig. S2 and has been re-used for comparison.

248

249 **3. Cells devoid of microtubules undergo fission with increased frequency but**
250 **show unaltered fusion frequencies**

251 While the Klp5Δ/Klp6Δ cells containing long microtubules had the same total
252 volume of mitochondria as WT cells (Fig. 1D), their mitochondria appeared less
253 fragmented. So, to specifically test the role of microtubules in dictating mitochondrial
254 fission, we depolymerized microtubules in wild-type and Klp5Δ/Klp6Δ cells and
255 measured mitochondrial dynamics in time-lapse movies (Fig. 3A, Movies S8, S9). In
256 both WT and Klp5Δ/Klp6Δ cells, upon microtubule depolymerization, we observed a
257 progressive increase in the number of mitochondria (Fig. 3B). We next quantified the
258 fission and fusion events in WT and Klp5Δ/Klp6Δ cells treated with MBC. We
259 measured that the fission frequency of mitochondria in MBC-treated cells was
260 doubled when compared to untreated control cells (Fig. 3C). At the same time, the
261 mitochondrial fusion frequency remained unchanged (Fig. 3D), indicating that the
262 immediate consequence of the loss of microtubules was increased fission, without
263 concomitant changes in mitochondrial fusion. Additionally, upon MBC treatment we
264 measured mitochondrial sizes and morphologies that were reminiscent of Klp4Δ cells
265 (Fig. 3E, Fig. S3A-C).

266 Increase in oxidative stress via reactive oxygen species (ROS) levels has also
267 been described to induce mitochondrial fission (Pletjushkina et al., 2006). However,
268 we measured no difference in ROS levels between wild-type, Klp5Δ/Klp6Δ, and
269 Klp4Δ cells (Fig. S3D).

270 **4. Mitochondria undergo stochastic partitioning during mitosis**

271 We next sought to understand the biological role for increased mitochondrial
272 fission upon microtubule depolymerization. Fission yeast undergoes closed mitosis,
273 wherein the nuclear envelope does not undergo breakdown during cell division (Ding
274 et al., 1997). Upon onset of mitosis in fission yeast, the interphase microtubules that
275 were previously in the cytoplasm are reorganized to form the spindle inside the
276 closed nucleus. This natural situation mimics the depolymerization of microtubules
277 via the chemical inhibitor MBC. Therefore, we set out to study the changes in the
278 mitochondrial network upon cell entry into mitosis. We first obtained high-resolution
279 deconvolved images of the microtubule and mitochondria in fission yeast cells
280 undergoing cell division (Fig. 4A, Fig. S4A, Movie S10). We observed that dividing
281 wild-type cells had ~4x the number of mitochondria in interphase cells (Fig. 4B).
282 Moreover, similar to what was seen in cells lacking microtubules or Klp4 (Fig. 1A),
283 mitochondria in dividing cells were shorter and more rounded (Fig. 4A, Fig. S4A).
284 There was no relationship between length of the mitotic spindle and the number of
285 mitochondria (Fig. 4B, Fig. S4A), indicating that the increased fission likely occurred
286 fairly early upon entry into mitosis. Analysis of time-lapse videos of wild-type cells
287 before and 10min after entry into mitosis revealed a doubling of mitochondrial
288 numbers in this time (Fig. 4C, D, Movie S11). The fragmented mitochondria
289 appeared more mobile and were able to traverse distances of ~1μm in the cell (Fig.

290 4C). In this same period of time, non-dividing interphase cells did not show any

291 change in mitochondrial numbers (Fig. S4B, C).

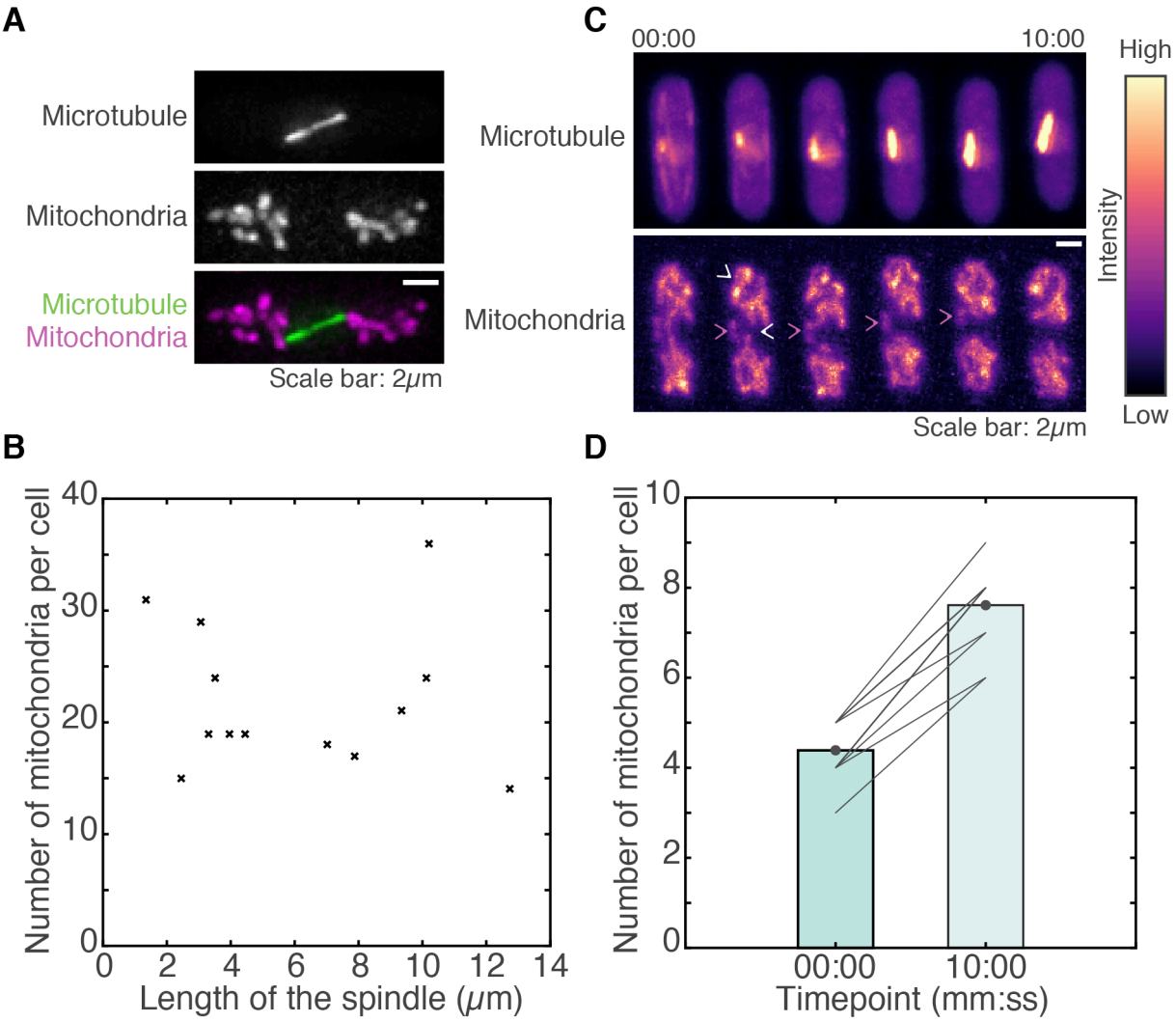

Figure 4. Mitotic cells contain several short mitochondria. (A) Maximum intensity projections of deconvolved Z-stack images of the microtubules (top), mitochondria (centre) and their composite (bottom) of a wild-type cell (strain KI001, see Table S1) undergoing division. **(B)** Scatter plot of the length of the mitotic spindle vs. the number of mitochondria per cell in dividing cells (*n*=13 cells). **(C)** Montage of maximum intensity projected confocal Z-stack images of the microtubules (top) and mitochondria (bottom) in a wild-type cell undergoing cell division represented in the intensity map indicated to the right of the images. White open arrowheads point to representative fission events. Magenta arrowheads point to a representative mobile, fragmented mitochondrion. Time is indicated above the images in mm:ss. **(D)** Bar plot of the mean number of mitochondria per cell before ('00:00') and 10mins after

('10:00') the onset of mitosis. Solid grey lines represent data from individual cells (*n*=16 cells).

292

293 Increase in mitochondrial numbers prior to cell division could aid in increasing
294 the likelihood of equal partitioning of mitochondria between daughter cells, given a
295 stochastic mechanism. To test if mitochondria in our system underwent stochastic,
296 independent segregation (Huh and Paulsson, 2011), with each mitochondrion in the
297 mother cell having a 50% chance of segregating to either of the future daughter cells
298 during mitosis, we tested the fit of our data to a binomial distribution (Birky, 1983)
299 using a Chi-square test as previously described (Hennis and Birky, 1984). Our data
300 (Table S2) did not differ significantly from a binomial distribution with a Chi-square
301 statistic of 7.1846 with 3 degrees of freedom and p=0.0662, indicating that
302 mitochondria in fission yeast were indeed segregating stochastically during cell
303 division. The increase in mitochondrial numbers upon onset of mitosis also served to
304 reduce the partitioning error of mitochondria between the daughter cells as predicted
305 by stochastic segregation (Fig. S4D).

306 **5. Cells with long microtubules are protected from unopposed mitochondrial**
307 **fission**

308 The mitochondrial fission protein in yeast is a dynamin-related GTPase, Dnm1
309 (Jourdain et al., 2009). Dnm1 brings about the fission of mitochondria by self-
310 assembling into rings or spirals around the mitochondrial outer membrane and
311 employing its GTPase activity to effect the scission (Ingerman et al., 2005). In the
312 absence of Dnm1, mitochondria are organised as extended, fused 'nets' (Guillou et
313 al., 2005; Jourdain et al., 2009), which do not undergo fission even in the absence of
314 microtubules (Fig. S5A). Further in Klp4Δ cells, which typically contain several short
315 mitochondria (Fig. 1A), absence of Dnm1 results in a single large, fused

316 mitochondrion (Fig. S5B). Therefore, all mitochondrial fission in *S. pombe* is reliant
317 on the activity of Dnm1. Additionally, during mitosis, cells lacking Dnm1 that
318 contained a single large mitochondrion relied on the cytokinesis of the mother cell to
319 also split the mitochondrion into the daughter cells (Fig. S5C).

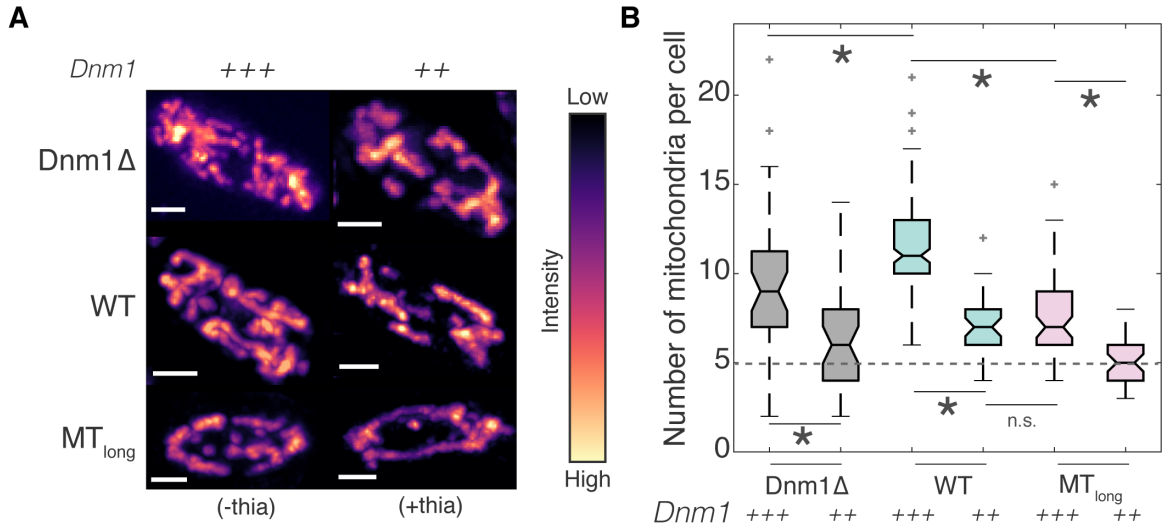

Figure 5. Association with microtubules prevents unopposed fission of mitochondria. (A) Maximum intensity projections of deconvolved Z-stack images of mitochondria in cells transformed with functional untagged Dnm1 (plasmid pREP41-Dnm1, see Table S1) in Dnm1Δ cells (see Table S1), wild-type ('WT', strain FY7143, see Table S1) and Klp5Δ/Klp6Δ cells ('MT_{long}', strain FY20823, see Table S1) represented in the intensity map indicated to the right of the images. High overexpression of Dnm1 is indicated with '+++' ('(-thia)') and low overexpression with '++' ('+thia)'). Scale bars represent 2μm**. (B)** Box plot of mitochondrial numbers in Dnm1Δ, WT and MT_{long} cells with high overexpression ('+++') or low expression of Dnm1 ('++') (*n*= 37, 36, 149, 37, 63, 41 cells respectively). The mean mitochondrial number in WT cells expressing normal amount of Dnm1 is depicted by the dashed line. Light grey crosses represent outliers, asterisk represents significance ($p<0.05$) and 'n.s.' indicates no significant difference (Kruskal-Wallis test, Tukey's Honestly Significant Difference Procedure).

320

321 Taken together, our results suggest that association of mitochondria with
322 microtubules inhibits mitochondrial fission. Previously, cryo-electron tomographic

323 analysis in fission yeast indicated a preferred separation distance of ~20nm for
324 mitochondria associated with microtubules (Höög et al., 2007). So too, cryo-elctron
325 microscopy in budding yeast revealed that Dnm1 assembled into rings with an outer
326 diameter of 129nm and lumen diameter of 89nm, resulting in ~20nm-high structures
327 around mitochondria (Mears et al., 2011). Therefore, mitochondria associated with
328 microtubules might have insufficient space to accommodate the Dnm1 ring around
329 their diameter, thereby inhibiting fission due to simple physical constraints. To test
330 this hypothesis, we first transformed Dnm1Δ, wild-type, and Klp5Δ/Klp6Δ cells with a
331 plasmid expressing Dnm1 under the control of the nmt1 promoter (see Table S1)
332 and visualized the mitochondria (Fig. 5A). These cells exhibit high overexpression of
333 Dnm1 in the absence of thiamine, and low overexpression in the presence of 0.05μM
334 thiamine in the culture medium. We counted the number of mitochondria present in
335 these cells and estimated that Dnm1Δ cells contained 9.5 ± 0.7 and 6.4 ± 0.5
336 mitochondria (mean ± s.e.m) with high overexpression and low overexpression of
337 Dnm1 respectively (Fig. 5B). Wild-type cells highly overexpressing Dnm1 had 11.6 ±
338 0.2 mitochondria (mean ± s.e.m), which is twice that of wild-type cells expressing
339 normal levels of Dnm1 (Fig. 5B). The increase in mitochondrial numbers in these
340 cells is due to the increase in Dnm1 numbers, that likely accelerates the kinetics of
341 the Dnm1 ring formation and hence, mitochondrial fission. In wild-type cells that
342 were grown in the presence of thiamine, the mitochondrial number was 7 ± 0.3
343 (mean ± s.e.m.), presumably because of low overexpression of Dnm1.

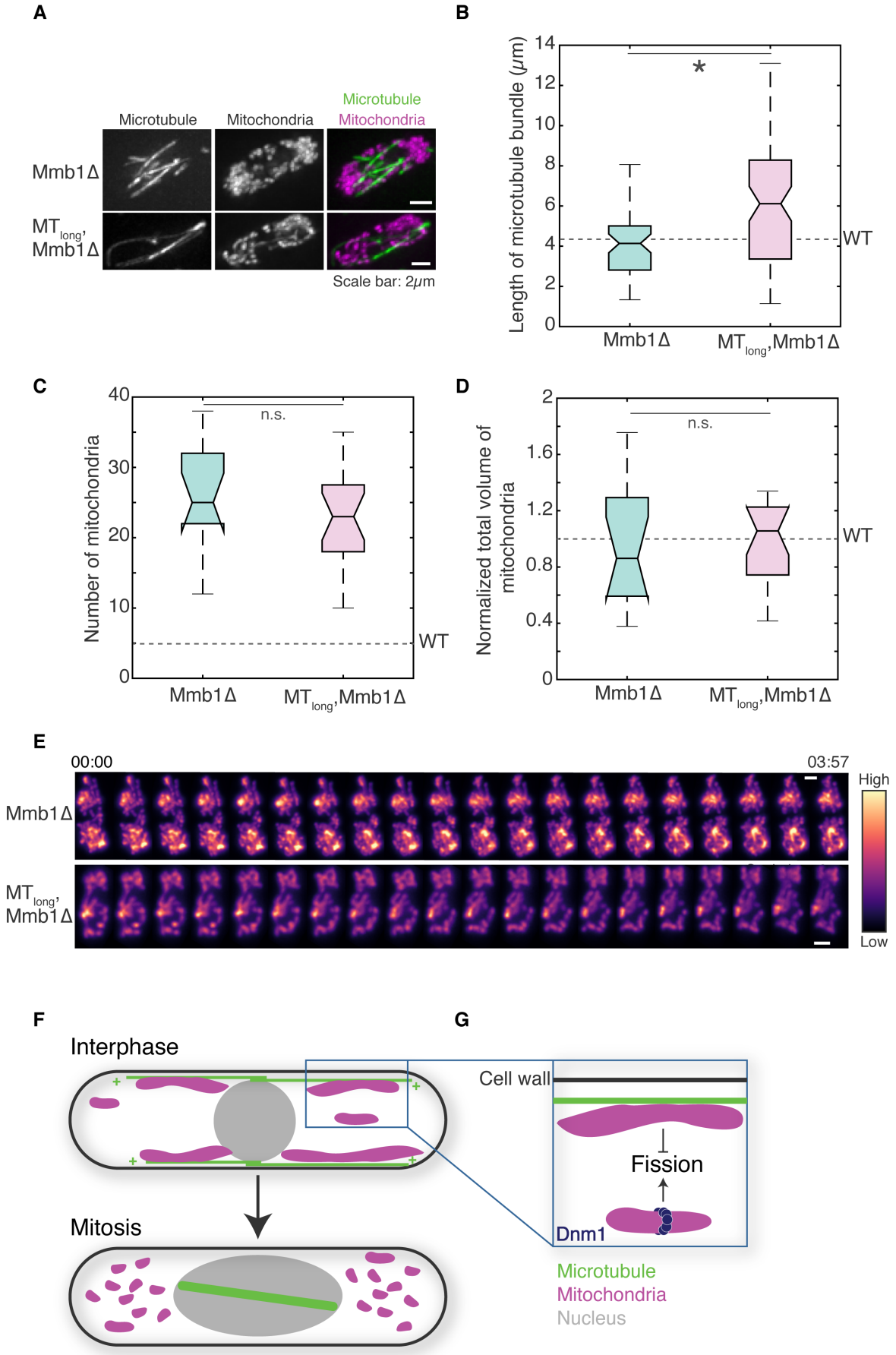
A
Microtubule
Mitochondria
Microtubule
Mitochondria
Mmb1Δ
MT long, Mmb1Δ
Scale bar: 2μm
B
Length of microtubule bundle (μm)
14
12
10
8
6
4
2
0
*
WT
Mmb1Δ
MT long, Mmb1Δ
C
Number of mitochondria
40
30
20
10
0
n.s.
WT
Mmb1Δ
MT long, Mmb1Δ
D
Normalized total volume of mitochondria
2
1.6
1.2
0.8
0.4
0
n.s.
WT
Mmb1Δ
MT long, Mmb1Δ
E
00:00
03:57
High
Low
Mmb1Δ
MT long, Mmb1Δ
F
Interphase
Mitosis
G
Cell wall
Fission
Dnm1
Microtubule
Mitochondria
Nucleus

344 **Figure 6. Deletion of Mmb1 results in unopposed fission in WT and MT_{long} cells.**
345 **(A)** Maximum intensity projections of deconvolved Z-stack images of microtubules
346 (left), mitochondria (centre) and their composite (right) in Mmb1Δ cells (top, strain
347 PT2244, see Table S1) and Klp5Δ/Klp6Δ-Mmb1Δ cells ('MT_{long}, Mmb1Δ', bottom,
348 strain VA076 see Table S1). **(B)** Box plot of microtubule bundle length in Mmb1Δ (*n*=
349 54 microtubules from 13 cells) and Klp5Δ/Klp6Δ-Mmb1Δ cells (*n*=81 microtubules
350 from 25 cells respectively). The mean microtubule bundle length in WT cells is
351 depicted by the dashed line. **(C)** Box plot of mitochondrial numbers in Mmb1Δ and
352 Klp5Δ/Klp6Δ-Mmb1Δ cells (*n*=14 and 20 cells respectively). The mean mitochondrial
353 number in WT cells is depicted by the dashed line. **(D)** Box plot of mitochondrial
354 volume in Mmb1Δ and Klp5Δ/Klp6Δ-Mmb1Δ cells (*n*=14 and 20 cells respectively)
355 normalized to mean total mitochondrial volume in WT cells. The mean mitochondrial
356 volume in WT cells is depicted by the dashed line. **(E)** Montage of maximum intensity
357 projected confocal Z-stack images of the mitochondria in a Mmb1Δ cell (top) and
358 Klp5Δ/Klp6Δ-Mmb1Δ cell ('MT_{long}, Mmb1Δ', bottom). The intensity map is indicated
359 to the right of the images. Time is indicated above the images in mm:ss. In B-D,
360 asterisk represents significance ($p<0.05$), 'n.s.' represents no significant difference
361 (one-way ANOVA, Tukey's Honestly Significant Difference Procedure). **(F)** Model of
362 mitochondrial dynamics mediated by microtubule dynamics. Microtubules polymerize
363 and depolymerize at their plus ends ('+'). Absence of microtubule bundles in the
364 cytoplasm during cell division enables the fragmentation of mitochondria. **(G)** When
365 mitochondria are bound to microtubules, Dnm1 assembly is inhibited. Upon
366 microtubule depolymerization, this inhibition is alleviated and Dnm1 can effectively
367 mediate scission of mitochondria.
368
369 Interestingly, in Klp5Δ/Klp6Δ cells with high and low overexpression of Dnm1,
370 we counted only 7.5 ± 0.3 mitochondria and 5.2 ± 0.2 mitochondria (mean ± s.e.m.)
371 respectively. In Klp5Δ/Klp6Δ, the presence of longer microtubules than wild-type
372 cells possibly prevented increased fission of mitochondria even when cells
373 overexpressed Dnm1. In fact, in Klp5Δ/Klp6Δ cells where there was low
374 overexpression of Dnm1, the mitochondrial number was comparable to that in wild-
375 type cells expressing normal levels of Dnm1 (Fig. 5B).

376 We additionally employed cells expressing mCherry-tagged microtubules,
377 GFP-tagged Dnm1 and Mitotracker-stained mitochondria and visualized the
378 localization of Dnm1 with respect to the microtubules and mitochondria in the same
379 cells (Fig. S6A). While 97.5% of Dnm1 spots colocalized with the mitochondria that
380 were not bound to the microtubule (115 out of 118 spots, n=18 cells), only 10.2% (12
381 out of 118 spots, n=18 cells) localized on mitochondria that were attached to the
382 microtubule. While these results indicated an inhibitory role for microtubule-
383 mitochondrial interactions in Dnm1 assembly, the non-functionality of fluorescently-
384 tagged Dnm1, that has been documented in other literature (Jourdain et al., 2009),
385 prevented direct visualization of fission of mitochondria by Dnm1 in these cells.

386 **6. Dissociation of mitochondria from microtubules leads to unopposed fission**

387 To further test the hypothesis that Dnm1 assembly was physically impeded on
388 microtubule-bound mitochondria, we sought to move microtubules and mitochondria
389 apart without perturbing the microtubule cytoskeleton. To this end, we employed
390 cells devoid of the protein that links mitochondria with microtubules in fission yeast,
391 Mmb1 (Fig. 6A, Movies S12, S13). First, we measured microtubule bundle lengths in
392 Mmb1Δ cells and Klp5Δ/Klp6Δ-Mmb1Δ cells. We did not observe a significant
393 difference in microtubule bundle lengths between WT and Mmb1Δ cells (Fig. 6B), but
394 Klp5Δ/Klp6Δ-Mmb1Δ cells exhibited microtubules that were significantly longer than
395 WT and Mmb1Δ cells, comparable to Klp5Δ/Klp6Δ cells.

396 Next, we counted 26.2 ± 1.8 (mean ± s.e.m.) mitochondria in these cells,
397 which is significantly higher than that in WT cells (Fig. 6C). In the case of
398 Klp5Δ/Klp6Δ-Mmb1Δ cells, although microtubules are significantly longer than in WT
399 cells (Fig. 6B), the absence of the linker between microtubules and mitochondria
400 resulted in extensive fission of mitochondria.

401 We counted 23.3 ± 1.4 (mean ± s.e.m.) mitochondria in Klp5Δ/Klp6Δ cells
402 lacking Mmb1Δ (Fig. 6C), which was not significantly different from Mmb1Δ cells.
403 Additionally, the total mitochondrial volume in both Mmb1Δ and Mmb1Δ-Klp5Δ/Klp6Δ
404 cells was also unchanged compared to WT cells indicating a change in morphology
405 of mitochondria, but not biogenesis (Fig. 6D). Time-lapse images of mitochondria in
406 Mmb1Δ and Mmb1Δ-Klp5Δ/Klp6Δ cells revealed mobile mitochondrial fragments,
407 consistent with the movement expected for mitochondria that are not bound to
408 microtubules (Fig. 6E). Therefore, by separating mitochondria from microtubules, we
409 alleviated the inhibition of Dnm1 assembly on the mitochondria, thereby promoting
410 mitochondrial fission.

411 Fig. S6B contains a summary of the mitochondrial parameters measured in
412 this study.

413 **Discussion**

414 We discovered that association with microtubules determines mitochondrial
415 dynamics and thereby, mitochondrial morphology (Fig. 6F). While previous studies
416 discounted the role of motors in the determination of mitochondrial positioning in
417 fission yeast (Brazer et al., 2000; Chiron et al., 2008; Li et al., 2015; Yaffe et al.,
418 2003), we have identified kinesin-like proteins that regulate mitochondrial
419 morphology through their control over microtubule length. The association of
420 mitochondria with microtubules mediated by the protein Mmb1 was found to be
421 necessary and sufficient to maintain equilibrium between fission and fusion of
422 mitochondria, with loss of Mmb1 leading to unopposed fission.

423 In mammalian cells, mitochondria employ microtubule-associated machinery
424 primarily to traverse the cell. However, mitochondrial dynamics have been observed
425 to be related to microtubule-assisted processes. For instance, in HeLa cells, Drp1

426 recruitment to the mitochondria was observed to be dependent on the motor protein
427 cytoplasmic dynein (Varadi et al., 2004). Mobile mitochondria on microtubules have
428 also been seen to participate in kiss-and-run fusions that are transient (Liu et al.,
429 2009). However, a direct role for the microtubule cytoskeleton in the maintenance of
430 mitochondrial dynamics has not yet been explored.

431 We observed that fission yeast cells fragment mitochondria by emptying the
432 cytoplasm of its microtubules upon onset of mitosis, thereby ensuring stochastic
433 partitioning (Birky, 1983) of the several small mitochondria between future daughter
434 cell. The increase in mitochondrial numbers prior to cell division likely serves to
435 create a well-mixed, homogeneous cytoplasm that is primed for stochastic
436 segregation of mitochondria (Fig. 6F). Mitochondrial fragmentation also reduces the
437 partitioning error between the daughter cells (Hennis and Birky, 1984), since
438 mitochondrial numbers of 5 or less, which is typical of wild-type interphase cells,
439 exhibit errors between ~45 and 100% (Fig. S4D). While mammalian cells also exhibit
440 fragmented mitochondria during mitosis (Mitra et al., 2009; Taguchi et al., 2007), it
441 has not yet been conclusively demonstrated that segregation to daughter cells is
442 achieved by stochastic mechanisms. As we observed here, in cells containing
443 mutants of the mitochondrial fission protein, mammalian cells employ the cytokinesis
444 machinery to partition mitochondria between daughter cells (Ishihara et al., 2009).
445 However, this mechanism of mitochondrial partitioning in Drp1-mutant cells is less
446 uniform since mitochondria exist as a large network at the time of division (Mishra
447 and Chan, 2014).

448 We observed that the presence of long microtubules was inhibitory for fission
449 of mitochondria even while Dnm1 was overexpressed. Wild-type cells contained the
450 same total volume of mitochondria as cells with long microtubules, but exhibited

451 increased mitochondrial fission in the presence of increased Dnm1 levels. In disease
452 states such as cancer (Ferreira-da-Silva et al., 2015) and neurodegeneration (Itoh et
453 al., 2013), mitochondrial fragmentation has been linked with overexpression of Drp1
454 in mammalian cells. In this work, we have identified that cells that present increased
455 microtubule stabilization are able to overcome the effect of Dnm1 overexpression.

456 By dissociating mitochondria from microtubules without perturbing the
457 microtubule cytoskeleton, we demonstrated that the failure of Dnm1 ring assembly in
458 the presence of microtubules was the nexus between microtubule dynamics and
459 mitochondrial dynamics (Fig. 6G). This finding could have interesting implications for
460 the interactions between microtubules and mitochondria in other cell types, including
461 in neurons where at any given time, a majority of the mitochondria are seemingly
462 stably attached to the microtubule cytoskeleton (Kang et al., 2008). Future studies in
463 these cells will illuminate the consequence of microtubule-binding on mitochondrial
464 dynamics.

465 Alternatively, increased fission upon microtubule depolymerization might be
466 brought about by phosphorylation of the mitochondrial fission protein Dnm1.
467 Mammalian Drp1 undergoes phosphorylation at S616 mediated by Cdk1/cyclin B
468 during cell division and increases mitochondrial fission (Taguchi et al., 2007).
469 However, fission yeast Dnm1 however lacks this phosphorylation site. Drp1 also
470 contains another phosphorylation site at S637, which is conserved in Dnm1.
471 However, PKA-mediated phosphorylation at S637 has been shown to inhibit fission
472 by Drp1 (Chang and Blackstone, 2007), whereas Ca++/calmodulin-dependent
473 protein kinase α-dependent phosphorylation of Drp1 S637 in rat hippocampal
474 neurons was shown to increase fission (Han et al., 2008). To date, yeast Dnm1 has
475 not been demonstrated to undergo phosphorylation at this site.

476 Another possibility is that there exists that an unidentified Dnm1-activating
477 factor that is sequestered by microtubules. This could explain the increase in
478 mitochondrial fragmentation upon microtubule depolymerization. However, in our
479 experiments with cells lacking Mmb1, we induced mitochondrial fragmentation by
480 dissociating mitochondria from microtubules without affecting the microtubule
481 cytoskeleton. Therefore, it is unlikely that mitochondrial fission is promoted by a
482 factor released upon microtubule depolymerization. In conclusion, we have
483 discovered a novel mechanism of regulation of mitochondrial fission by the physical
484 association of mitochondria with microtubules.

485

486 **References**

487 Ashrafian, H., Docherty, L., Leo, V., Towlson, C., Neilan, M., Steeples, V., Lygate,
488 C.A., Hough, T., Townsend, S., Williams, D., et al. (2010). A Mutation in the
489 Mitochondrial Fission Gene Dnm1l Leads to Cardiomyopathy. PLoS Genet. *6*,
490 e1001000.
491 Basu, K., Lajoie, D., Aumentado-Armstrong, T., Chen, J., Koning, R.I., Bossy, B.,
492 Bostina, M., Sik, A., Bossy-Wetzel, E., and Rouiller, I. (2017). Molecular mechanism
493 of DRP1 assembly studied in vitro by cryo-electron microscopy. PLoS One *12*,
494 e0179397.
495 Bergeland, T., Widerberg, J., Bakke, O., and Nordeng, T.W. (2001). Mitotic
496 partitioning of endosomes and lysosomes. Curr. Biol. *11*, 644–651.
497 Birky, C.W. (1983). The partitioning of cytoplasmic organelles at cell division. Int.
498 Rev. Cytol. Suppl. *15*, 49–89.
499 Bleazard, W., McCaffery, J.M., King, E.J., Bale, S., Mozdy, A., Tieu, Q., Nunnari, J.,
500 and Shaw, J.M. (1999). The dynamin-related GTPase Dnm1 regulates mitochondrial
501 fission in yeast. Nat. Cell Biol. *1*, 298–304.
502 Brazer, S.W., Williams, H.P., and Chappell, T.G. (2000). A fission yeast kinesin
503 affects Golgi membrane recycling. 149–166.
504 Browning, H., Hayles, J., Mata, J., Aveline, L., Nurse, P., and McIntosh, J.R. (2000).
505 Tea2p is a kinesin-like protein required to generate polarized growth in fission yeast.

506 J. Cell Biol. *151*, 15–28.
507 Busch, K.E., Hayles, J., Nurse, P., and Brunner, D. (2004). Tea2p Kinesin Is
508 Involved in Spatial Microtubule Organization by Transporting Tip1p on Microtubules.
509 Dev. Cell *6*, 831–843.
510 Chang, C.-R., and Blackstone, C. (2007). Cyclic AMP-dependent protein kinase
511 phosphorylation of Drp1 regulates its GTPase activity and mitochondrial morphology.
512 J. Biol. Chem. *282*, 21583–21587.
513 Chen, H., and Chan, D.C. (2009). Mitochondrial dynamics--fusion, fission,
514 movement, and mitophagy--in neurodegenerative diseases. Hum. Mol. Genet. *18*,
515 R169-76.
516 Chen, Y., and Sheng, Z.-H. (2013). Kinesin-1-syntaphilin coupling mediates activity-
517 dependent regulation of axonal mitochondrial transport. J. Cell Biol. *202*, 351–364.
518 Chiron, S., Bobkova, A., Zhou, H., and Yaffe, M.P. (2008). CLASP regulates
519 mitochondrial distribution in Schizosaccharomyces pombe. J. Cell Biol. *182*, 41–49.
520 Delettre, C., Lenaers, G., Griffoin, J.-M., Gigarel, N., Lorenzo, C., Belenguer, P.,
521 Pelloquin, L., Grosgeorge, J., Turc-Carel, C., Perret, E., et al. (2000). Nuclear gene
522 OPA1, encoding a mitochondrial dynamin-related protein, is mutated in dominant
523 optic atrophy. Nat. Genet. *26*, 207–210.
524 Deng, H., Dodson, M.W., Huang, H., and Guo, M. (2008). The Parkinson's disease
525 genes pink1 and parkin promote mitochondrial fission and/or inhibit fusion in
526 Drosophila. Proc. Natl. Acad. Sci. *105*, 14503–14508.
527 Ding, R., West, R.R., Morphew, D.M., Oakley, B.R., and McIntosh, J.R. (1997). The
528 spindle pole body of Schizosaccharomyces pombe enters and leaves the nuclear
529 envelope as the cell cycle proceeds. Mol. Biol. Cell *8*, 1461–1479.
530 Eura, Y., Ishihara, N., Yokota, S., and Mihara, K. (2003). Two Mitofusin Proteins,
531 Mammalian Homologues of FZO, with Distinct Functions Are Both Required for
532 Mitochondrial Fusion. J. Biochem. *134*, 333–344.
533 Fehrenbacher, K.L., Yang, H., Gay, A.C., Huckaba, T.M., and Pon, L.A. (2004). Live
534 Cell Imaging of Mitochondrial Movement along Actin Cables in Budding Yeast. Curr.
535 Biol. *14*, 1996–2004.
536 Ferreira-da-Silva, A., Valacca, C., Rios, E., Pópulo, H., Soares, P., Sobrinho-
537 Simões, M., Scorrano, L., Máximo, V., and Campello, S. (2015). Mitochondrial
538 Dynamics Protein Drp1 Is Overexpressed in Oncocytic Thyroid Tumors and
539 Regulates Cancer Cell Migration. PLoS One *10*, e0122308.

540 Forsburg, S.L., and Rhind, N. (2006). Basic methods for fission yeast. Yeast *23*,
541 173–183.
542 Fu, C., Jain, D., Costa, J., Velve-Casquillas, G., and Tran, P.T. (2011). Mmb1p binds
543 mitochondria to dynamic microtubules. Curr. Biol. *21*, 1431–1439.
544 Glater, E.E., Megeath, L.J., Stowers, R.S., and Schwarz, T.L. (2006). Axonal
545 transport of mitochondria requires milton to recruit kinesin heavy chain and is light
546 chain independent. J. Cell Biol. *173*, 545–557.
547 Graves, J.A., Wang, Y., Sims-Lucas, S., Cherok, E., Rothermund, K., Branca, M.F.,
548 Elster, J., Beer-Stolz, D., Van Houten, B., Vockley, J., et al. (2012). Mitochondrial
549 Structure, Function and Dynamics Are Temporally Controlled by c-Myc. PLoS One *7*,
550 e37699.
551 Guillou, E., Bousquet, C., Daloyau, M., Emorine, L.J., and Belenguer, P. (2005).
552 Msp1p is an intermembrane space dynamin-related protein that mediates
553 mitochondrial fusion in a Dnm1p-dependent manner in S. pombe. FEBS Lett. *579*,
554 1109–1116.
555 Han, X.-J., Lu, Y.-F., Li, S.-A., Kaitsuka, T., Sato, Y., Tomizawa, K., Nairn, A.C.,
556 Takei, K., Matsui, H., and Matsushita, M. (2008). CaM kinase Iα–induced
557 phosphorylation of Drp1 regulates mitochondrial morphology. J. Cell Biol. *182*, 573–
558 585.
559 Hennis, A.S., and Birky, C.W. (1984). Stochastic partitioning of chloroplasts at cell
560 division in the alga Olisthodiscus, and compensating control of chloroplast
561 replication. J. Cell Sci. *70*, 1–15.
562 Hermann, G.J., Thatcher, J.W., Mills, J.P., Hales, K.G., Fuller, M.T., Nunnari, J., and
563 Shaw, J.M. (1998). Mitochondrial fusion in yeast requires the transmembrane
564 GTPase Fzo1p. J. Cell Biol. *143*, 359–373.
565 Hirai, K., Aliev, G., Nunomura, A., Fujioka, H., Russell, R.L., Atwood, C.S., Johnson,
566 A.B., Kress, Y., Vinters, H. V, Tabaton, M., et al. (2001). Mitochondrial abnormalities
567 in Alzheimer's disease. J. Neurosci. *21*, 3017–3023.
568 Höög, J.L., Schwartz, C., Noon, A.T., O'Toole, E.T., Mastronarde, D.N., McIntosh,
569 J.R., and Antony, C. (2007). Organization of interphase microtubules in fission yeast
570 analyzed by electron tomography. Dev. Cell *12*, 349–361.
571 Huh, D., and Paulsson, J. (2011). Random partitioning of molecules at cell division.
572 Proc. Natl. Acad. Sci. U. S. A. *108*, 15004–15009.
573 Ingerman, E., Perkins, E.M., Marino, M., Mears, J.A., McCaffery, J.M., Hinshaw,

574 J.E., and Nunnari, J. (2005). Dnm1 forms spirals that are structurally tailored to fit
575 mitochondria. J. Cell Biol. *170*, 1021–1027.
576 Ishihara, N., Nomura, M., Jofuku, A., Kato, H., Suzuki, S.O., Masuda, K., Otera, H.,
577 Nakanishi, Y., Nonaka, I., Goto, Y., et al. (2009). Mitochondrial fission factor Drp1 is
578 essential for embryonic development and synapse formation in mice. Nat. Cell Biol.
579 *11*, 958–966.
580 Itoh, K., Nakamura, K., Iijima, M., and Sesaki, H. (2013). Mitochondrial dynamics in
581 neurodegeneration. Trends Cell Biol. *23*, 64–71.
582 Jajoo, R., Jung, Y., Huh, D., Viana, M.P., Rafelski, S.M., Springer, M., and Paulsson,
583 J. (2016). Accurate concentration control of mitochondria and nucleoids. Science
584 (80-.). *351*, 169–172.
585 Jourdain, I., Gachet, Y., and Hyams, J.S. (2009). The dynamin related protein Dnm1
586 fragments mitochondria in a microtubule-dependent manner during the fission yeast
587 cell cycle. Cell Motil. Cytoskeleton *66*, 509–523.
588 Kang, J.-S., Tian, J.-H., Pan, P.-Y., Zald, P., Li, C., Deng, C., and Sheng, Z.-H.
589 (2008). Docking of Axonal Mitochondria by Syntaphilin Controls Their Mobility and
590 Affects Short-Term Facilitation. Cell *132*, 137–148.
591 Kanter-Smoler, G., Dahlkvist, A., and Sunnerhagen (1994). Improved Method for
592 rapid Transformation of Intact Schizosaccharomyces pombe cells. Biotechniques *16*,
593 798–800.
594 Krüger, N., and Tolic, I.M. (2008). Association of mitochondria with spindle poles
595 facilitates spindle alignment. Curr. Biol. *18*, 646–647.
596 Lawrence, E., and Mandato, C. (2013). Mitochondrial inheritance is mediated by
597 microtubules in mammalian cell division. Commun. Integr. Biol. *6*, e27557.
598 Li, T., Zheng, F., Cheung, M., Wang, F., and Fu, C. (2015). Fission yeast
599 mitochondria are distributed by dynamic microtubules in a motor-independent
600 manner. Sci. Rep. *5*, 11023.
601 Liu, X., Weaver, D., Shirihai, O., and Hajnóczky, G. (2009). Mitochondrial “kiss-and-
602 run”: interplay between mitochondrial motility and fusion-fission dynamics. EMBO J.
603 *28*, 3074–3089.
604 Mears, J.A., Lackner, L.L., Fang, S., Ingerman, E., Nunnari, J., and Hinshaw, J.E.
605 (2011). Conformational changes in Dnm1 support a contractile mechanism for
606 mitochondrial fission. Nat. Struct. Mol. Biol. *18*, 20–26.
607 Mishra, P., and Chan, D.C. (2014). Mitochondrial dynamics and inheritance during

608 cell division, development and disease. Nat. Rev. Mol. Cell Biol. *15*, 634–646.
609 Mishra, P., and Chan, D.C. (2016). Metabolic regulation of mitochondrial dynamics.
610 J. Cell Biol. *212*, 379–387.
611 Mitra, K., Wunder, C., Roysam, B., Lin, G., and Lippincott-Schwartz, J. (2009). A
612 hyperfused mitochondrial state achieved at G1-S regulates cyclin E buildup and
613 entry into S phase. Proc. Natl. Acad. Sci. U. S. A. *106*, 11960–11965.
614 Pilling, A.D., Horiuchi, D., Lively, C.M., and Saxton, W.M. (2006). Kinesin-1 and
615 Dynein are the primary motors for fast transport of mitochondria in Drosophila motor
616 axons. Mol. Biol. Cell *17*, 2057–2068.
617 Pletjushkina, O.Y., Lyamzaev, K.G., Popova, E.N., Nepryakhina, O.K., Ivanova,
618 O.Y., Domnina, L.V., Chernyak, B.V., and Skulachev, V.P. (2006). Effect of oxidative
619 stress on dynamics of mitochondrial reticulum. Biochim. Biophys. Acta - Bioenerg.
620 *1757*, 518–524.
621 Sesaki, H., Southard, S.M., Yaffe, M.P., and Jensen, R.E. (2003). Mgm1p, a
622 dynamin-related GTPase, is essential for fusion of the mitochondrial outer
623 membrane. Mol. Biol. Cell *14*, 2342–2356.
624 Shima, D.T., Cabrera-Poch, N., Pepperkok, R., and Warren, G. (1998). An ordered
625 inheritance strategy for the Golgi apparatus: visualization of mitotic disassembly
626 reveals a role for the mitotic spindle. J. Cell Biol. *141*, 955–966.
627 Smirnova, E., Griparic, L., Shurland, D.L., and van der Bliek, A.M. (2001). Dynamin-
628 related protein Drp1 is required for mitochondrial division in mammalian cells. Mol.
629 Biol. Cell *12*, 2245–2256.
630 Stowers, R.S., Megeath, L.J., Górska-Andrzejak, J., Meinertzhagen, I.A., and
631 Schwarz, T.L. (2002). Axonal transport of mitochondria to synapses depends on
632 milton, a novel Drosophila protein. Neuron *36*, 1063–1077.
633 Taguchi, N., Ishihara, N., Jofuku, A., Oka, T., and Mihara, K. (2007). Mitotic
634 phosphorylation of dynamin-related GTPase Drp1 participates in mitochondrial
635 fission. J. Biol. Chem. *282*, 11521–11529.
636 Tischer, C., Brunner, D., and Dogterom, M. (2009). Force- and kinesin-8-dependent
637 effects in the spatial regulation of fission yeast microtubule dynamics. Mol. Syst. Biol.
638 *5*, 250.
639 van Spronsen, M., Mikhaylova, M., Lipka, J., Schlager, M.A., van den Heuvel, D.J.,
640 Kuijpers, M., Wulf, P.S., Keijzer, N., Demmers, J., Kapitein, L.C., et al. (2013).
641 TRAK/Milton Motor-Adaptor Proteins Steer Mitochondrial Trafficking to Axons and

642 Dendrites. Neuron *77*, 485–502.
643 Varadi, A., Johnson-Cadwell, L.I., Cirulli, V., Yoon, Y., Allan, V.J., and Rutter, G.A.
644 (2004). Cytoplasmic dynein regulates the subcellular distribution of mitochondria by
645 controlling the recruitment of the fission factor dynamin-related protein-1. J. Cell Sci.
646 *117*, 4389–4400.
647 West, R.R., Malmstrom, T., Troxell, C.L., and McIntosh, J.R. (2001). Two related
648 kinesins, klp5+ and klp6+, foster microtubule disassembly and are required for
649 meiosis in fission yeast. Mol. Biol. Cell *12*, 3919–3932.
650 Yaffe, M.P., Stuurman, N., and Vale, R.D. (2003). Mitochondrial positioning in fission
651 yeast is driven by association with dynamic microtubules and mitotic spindle poles.
652 PNAS *100*, 11424–11428.
653

654 **Acknowledgments**

655 We thank J. M. Thankachan, S. S. Nuthalapati and M. Ayushman for pilot
656 experiments; High Content Imaging Facility at BSSE, IISc, and P. I. Rajyaguru for
657 the use of the InCell 6000, and Deltavision RT microscopes respectively; P. Delivani,
658 I. Jourdain, R.C. Salas, M. Takaine, I. Tolic, Y. Gachet, P. Tran, and NBRP Japan for
659 yeast strains and constructs; S. Jain for CellROX reagent. The research was
660 supported by the Department of Science and Technology (India)-INSPIRE Faculty
661 Award, the Department of Biotechnology (India) Innovative Young Biotechnologist
662 Award, and the Science and Engineering Research Board (SERB, India) Early
663 Career Research Award awarded to V.A., and SERB Early Career Research Award
664 awarded to S.J.

665

666

667 **Author contributions**

668 K.M. and L.A.C carried out and analyzed the Dnm1 and Mmb1 experiments, M.K.C.
669 and S. J. carried out and analyzed the flow cytometry experiments, V.A. performed

670 all the other experiments and data analysis, designed the project, and wrote the
671 paper.
672
673 **Competing interests**
674 The authors declare no competing financial interests.
675

676 **Supplementary Materials and Methods**

677 **ROS detection and viability assay using flow cytometry.** A loopful of L972,
678 FY20823 or McI438 cells were inoculated in liquid YE and incubated overnight at
679 30°C in a shaking incubator. Cells were harvested using a table-top centrifuge
680 (2000g, 30s) and washed three times with 1X PBS. The pellets were re-suspended
681 in 500µl of 1X PBS, containing CellROX (5µM) dye (ThermoFisher, USA). Following
682 incubation at 30°C for 30min, cells were washed three times with 1X PBS. Finally,
683 cell pellets were re-suspended in an appropriate volume of 1X PBS containing
684 propidium iodide (6µg/ml), incubated for 10min at room temperature, and run on a
685 flow cytometer (BD FACS-Celesta). A minimum of 10,000 events of cells was
686 collected, and data analyzed using FlowJo (FlowJo LLC, USA). ROS was reported
687 as median fluorescence intensity for each dataset.

688 **Estimation of partitioning error during cell division.** The partitioning error of
689 mitochondria at cell division between the daughter cells Q_x was calculated from the
690 equation (Huh and Paulsson, 2011):

691 $$Q_x^2 = \frac{(L-R)^2}{x^2}$$

692 where L and R were mitochondrial numbers in the resulting daughter cells and x, the
693 number of mitochondria in the mother cell. The data in Fig. S4D were simulated by
694 independently assigning x mitochondria with 50% probability to either daughter cell.
695 Simulations were re-run 50 times to obtain the mean and the standard error of the
696 mean depicted in Fig. S4D.

697 **Counting of Dnm1 spots.** Dnm1 was visualised in cells grown in the presence of
698 0.05µM thiamine for partial induction of the nmt1 promoter. Even with only partial
699 induction, a majority of the cells showed extremely high expression of Dnm1, with
700 most of the signal concentrated in a single spot in the cell. The rest of the cells

701 showed lower expression, with Dnm1 signal distributed in a few spots across the
702 cell. The latter were chosen for analysis of number of Dnm1 spots. For counting
703 Dnm1 spots, the maximum intensity projection of deconvolved Z-stack images were
704 used. For identification of spots, we set the lower threshold as 60-80% of the
705 maximum intensity in these images. The contrast in the images in Fig. S6B reflect
706 these threshold settings.
707

708 **Supplementary Tables**

Name	Phenotype	Source
Dnm1Δ	*h- dnm1::kanr leu1-32ade-*	Yannick Gachet, Toulouse
FY20823	*h- leu1 ura4 his7 Δklp5::ura4+ Δklp6::ura4+*	NBRP, Japan
FY7143	*h- ura4-D18 leu1-32 ade6-M216 his7-366*	Iva Tolić, Croatia
G3B	*h- Δklp5- Δklp6 – nmt1-GFP-atb2 leu ade*	Rafael Carazo Salas, UK
G5B	*h- klp4::kanr nmt1-GFP-atb2 leu ura*	Rafael Carazo Salas, UK
KI001	*h+ sid4-GFP::kanr kanr -nmtP3-GFP-atb2+ nmt1-pCOX4RFP::leu1+ ura4-D18 ade6-M210*	Iva Tolić, Croatia
L972	*h- WT*	Iva Tolić, Croatia
Mcl438	*h+ tea2d:his3 ade6 leu1-32 ura4-D18 his3-D1*	Iva Tolić, Croatia
MTY271	*h- mCherry-atb2:hphMX6 leu1-32 ura-d18*	Masakatsu Takaine, Japan
PT2244	*h+ mmb1Δ:Kanr cox4-GFP:leu2 mCherry-atb2:Hygr ade6-m210 leu1-32 ura4-d18*	Phong Tran, USA
PT1650	*h+ cox4-GFP:leu1 ade6-M210 leu1-32 ura4-D18*	Phong Tran, USA
VA076	*h+ mmb1Δ:Kanr cox4-GFP:leu2 mCherry-atb2:Hygr Δklp5::ura4+ Δklp6::ura4+ ade6-m210 his7*	This study
VA084	*h- dnm1::kanr klp4::kanr nmt1-GFP-atb2 leu1-32 ade-*	This study
FYP2026 (plasmid)	*nmt-GFP-atb2: LEU2*	NBRP, Japan
pREP41-Dnm1 (plasmid)	*Dnm1 (untagged)*	Isabelle Jourdain, UK
pREP41-Dnm1-Cterm-GFP (plasmid)	*Dnm1-GFP*	Isabelle Jourdain, UK

709

710 **Table S1. Strains and constructs used in this study**

n	*x*	*(n-x)*	*N*	*Obs.*	*Exp.*	*Obs.-Exp.*
5	2	3	2	2	1.25	0.75
6	2	4	2	2	0.94	1.06
	3	3		0	0.63	-0.63
7	4	3	3	3	1.64	1.36
8	2	6	7	1	1.53	-0.53
	3	5		4	3.06	0.94
	4	4		2	1.91	0.09
9	3	6	11	4	3.61	0.39
	4	5		7	5.41	1.59
10	3	7	6	1	1.41	-0.41
	4	6		2	2.46	-0.46
	5	5		3	1.48	1.52
11	4	7	4	1	1.29	-0.29
	5	6		3	1.80	1.20
12	5	7	8	6	3.09	2.91
	6	6		2	1.80	0.20
13	5	8	5	3	1.57	1.43
	6	7		2	2.09	-0.09
14	5	9	7	1	1.71	-0.71
	6	8		4	2.57	1.43
	7	7		2	1.47	0.53
15	6	9	5	2	1.53	0.47
	7	8		3	1.96	1.04
16	6	10	2	1	0.49	0.51
	7	9		1	0.70	0.30
	8	8		0	0.40	-0.40
17	6	11	2	1	0.38	0.62
	7	10		0	0.60	-0.60
	8	9		1	0.74	0.26
18	8	10	1	1	0.33	0.67
	9	9		0	0.37	-0.37

Table S2. Partitioning of mitochondria between daughter cells. *n* is the number of mitochondria in the mother, *x* and *n-x* in the daughter cells at cell division. *N* is the number of cells counted with *n* mitochondria in the mother. *Obs.* is the observed number of cells showing partition of *n* into *x* and *n-x*, and *Exp.* is the expected number of cells with the same *x* and *n-x* partition given *N* cells predicted by the binomial distribution.

Supplementary Figures

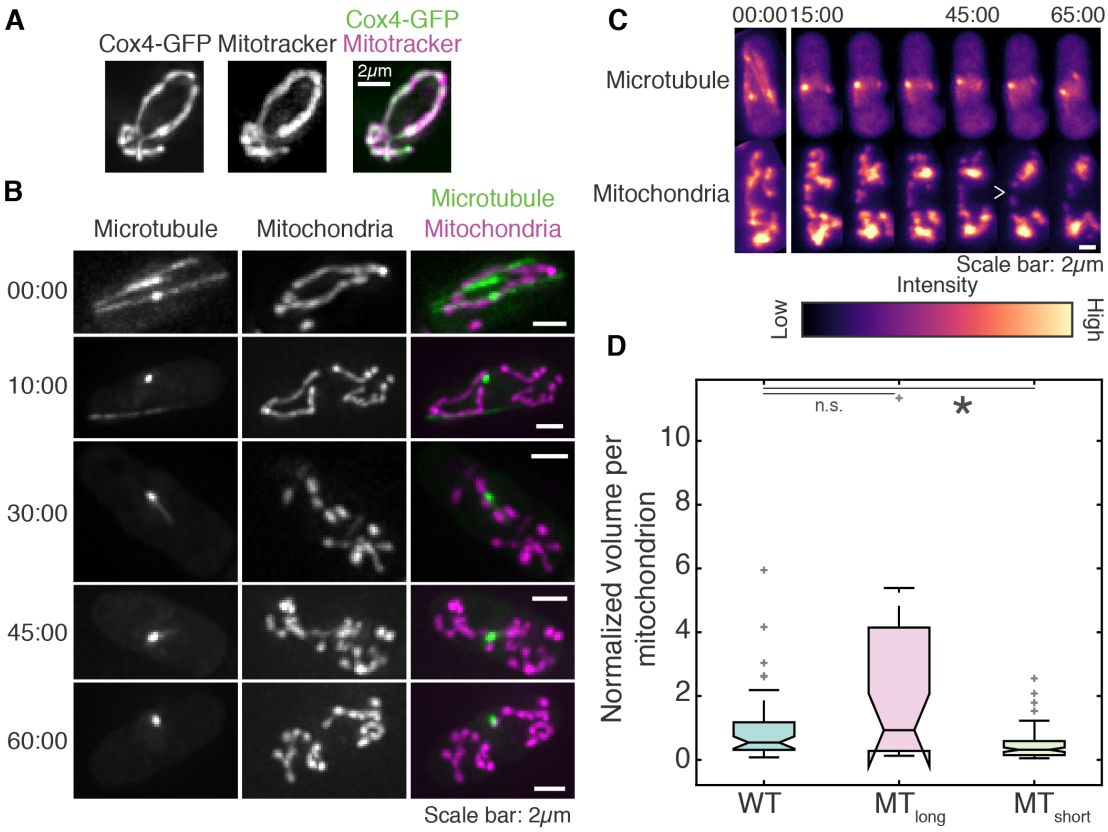

Figure S1. Depolymerization of microtubules increases mitochondrial fission. **(A)** Maximum intensity projections of deconvolved Z-stack images of Cox4-GFP (left), Mitotracker Orange staining (centre) and their composite (right) in interphase cells (strain PT1650, see Table S1) showing colocalization of both signal intensities. **(B)** Maximum intensity projections of deconvolved Z-stack images of microtubules (left), mitochondria (centre) and their composite (right) in fission yeast cells treated with MBC (strain KI001, see Methods). Time in mm:ss is indicated to the left of the images. **(C)** Montage of maximum intensity projected confocal Z-stack images of microtubule depolymerization (top) and mitochondria (bottom) of wild-type cells (strain KI001, see Table S1) treated with MBC (see Methods) represented in the intensity map indicated at the bottom of the images. The open white arrowhead indicates a representative fission event. **(D)** Box plot of the volume of individual mitochondria in wild-type ('WT'), Klp5Δ/Klp6Δ ('MT_{long}') and Klp4Δ ('MT_{short}') cells normalized to mean mitochondrial volume in wild-type cells (*n*=49, 28 and 100 mitochondria respectively). Light grey crosses represent outliers, asterisk represents

736 significance (p<0.05) and 'n.s.' indicates no significant difference (Kruskal-Wallis
737 test, Tukey's Honestly Significant Difference Procedure).

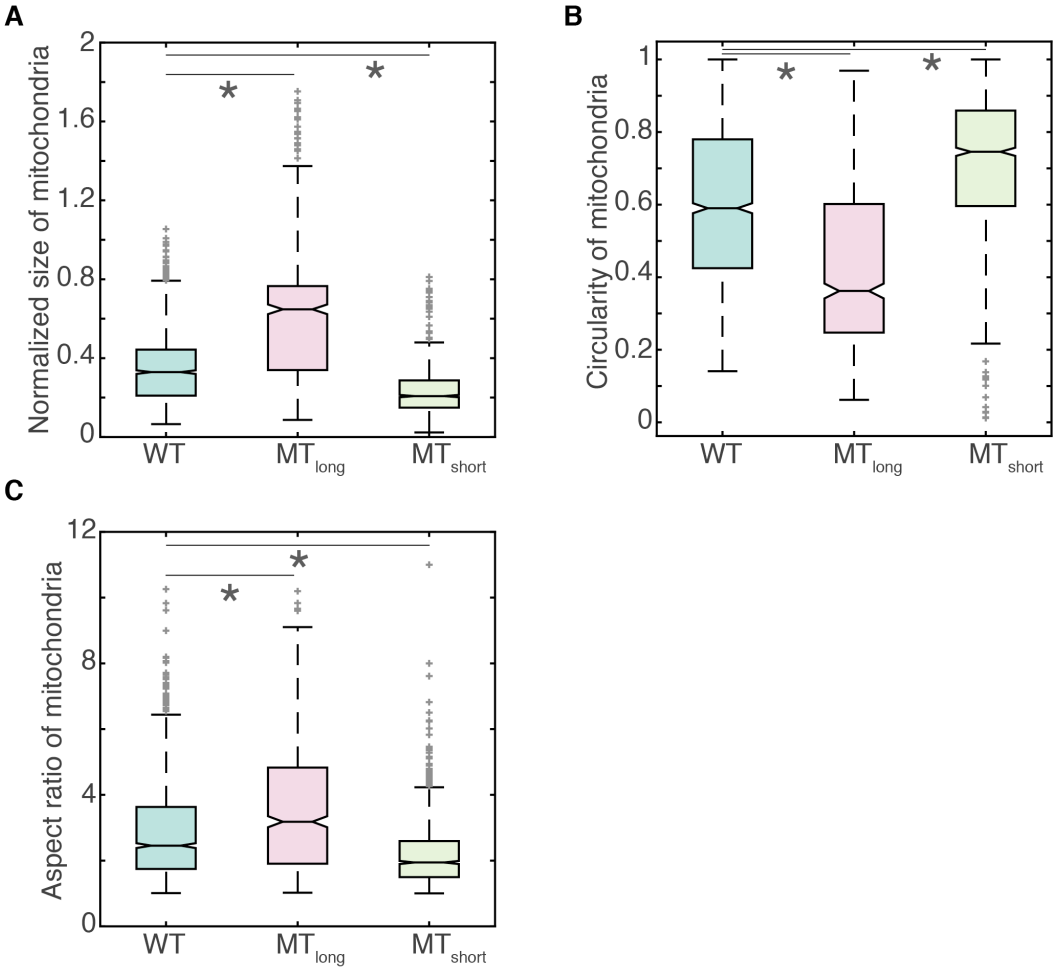

738

739 **Figure S2. Microtubule lengths determine the morphology of mitochondria. (A)**
740 Box plot of the size of individual mitochondria in wild-type ('WT'), Klp5Δ/Klp6Δ
741 ('MT_{long}') and Klp4Δ ('MT_{short}') cells normalized to their cell lengths (*n*=1613, 739 and
742 1326 mitochondria respectively). **(B)** Box plot of the circularity of mitochondria in WT,
743 MT_{long} and MT_{short} cells (*n*=1613, 739 and 1326 mitochondria respectively). **(C)** Box
744 plot of the aspect ratio of mitochondria in WT, MT_{long} and MT_{short} cells (*n*=1613, 739
745 and 1326 mitochondria respectively). In A-C, light grey crosses represent outliers,
746 asterisk represents significance (p<0.05) and 'n.s.' indicates no significant difference
747 (Kruskal-Wallis test, Tukey's Honestly Significant Difference Procedure).
748

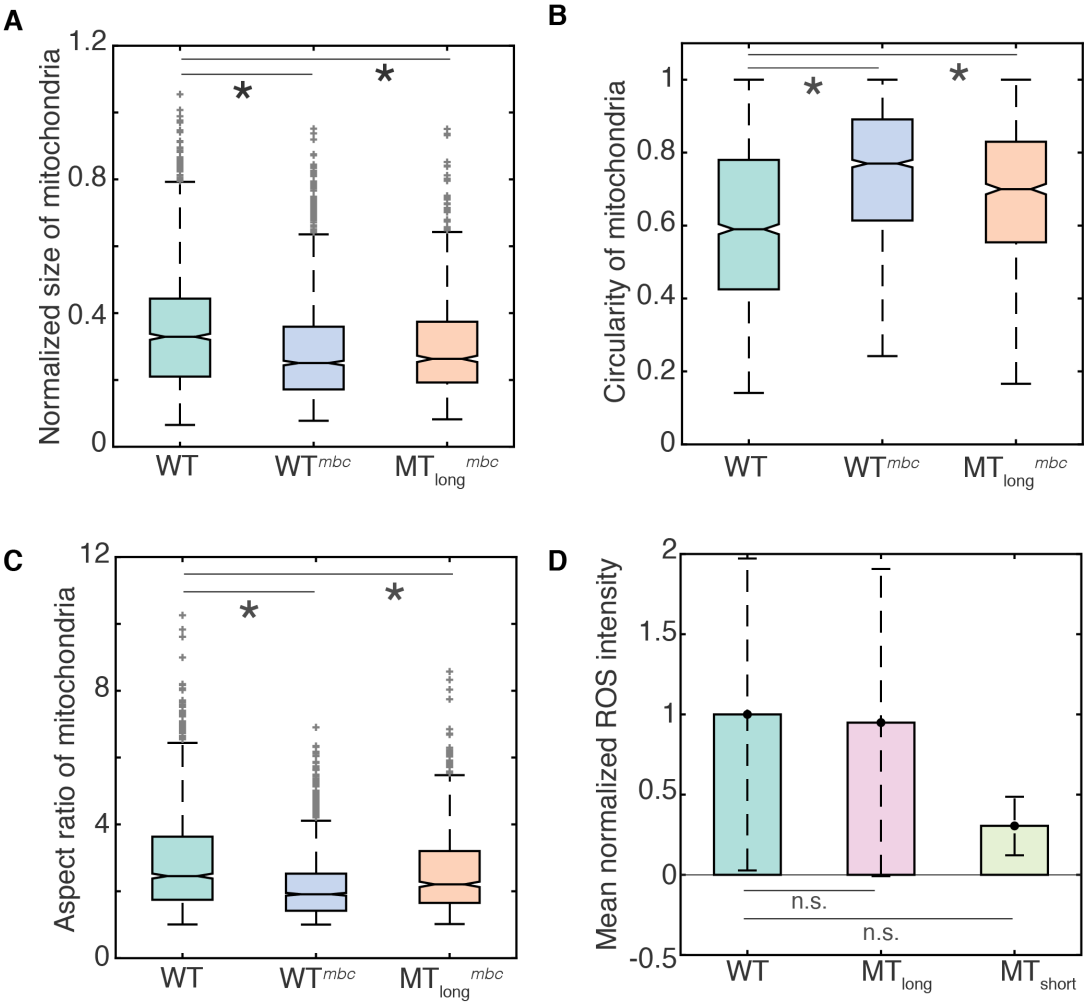

Figure S3. Morphology of mitochondria is altered by treatment with MBC. (A) Box plot of the size of individual mitochondria in WT, WT^{mbc}, and MT_{long}^{mbc} cells normalized to their cell lengths (*n*=1613, 1765 and 886 mitochondria respectively). **(B)** Box plot of the circularity of mitochondria in WT, WT^{mbc}, and MT_{long}^{mbc} cells (*n*=1613, 1765 and 886 mitochondria respectively). **(C)** Box plot of the aspect ratio of mitochondria in WT, WT^{mbc}, and MT_{long}^{mbc} cells (*n*=1613, 1765 and 886 mitochondria respectively). **(D)** Bar plot of cellular ROS measured using flow cytometry (see Supplementary Information) in live WT, MT_{long} and MT_{short} cells normalized to mean of the ROS intensity in WT cells (*n*=3 independent experiments, ≥10,000 events each). Error bars represent standard deviation. In A-D, light grey crosses represent outliers, asterisk represents significance ($p<0.05$) and 'n.s.' indicates no significant difference (Kruskal-Wallis test in A-C, one-way ANOVA in D, Tukey's Honestly Significant Difference Procedure). Note that the WT data represented in this figure is the identical to the wild-type data plotted in Fig. S2 and has been re-used for comparison.

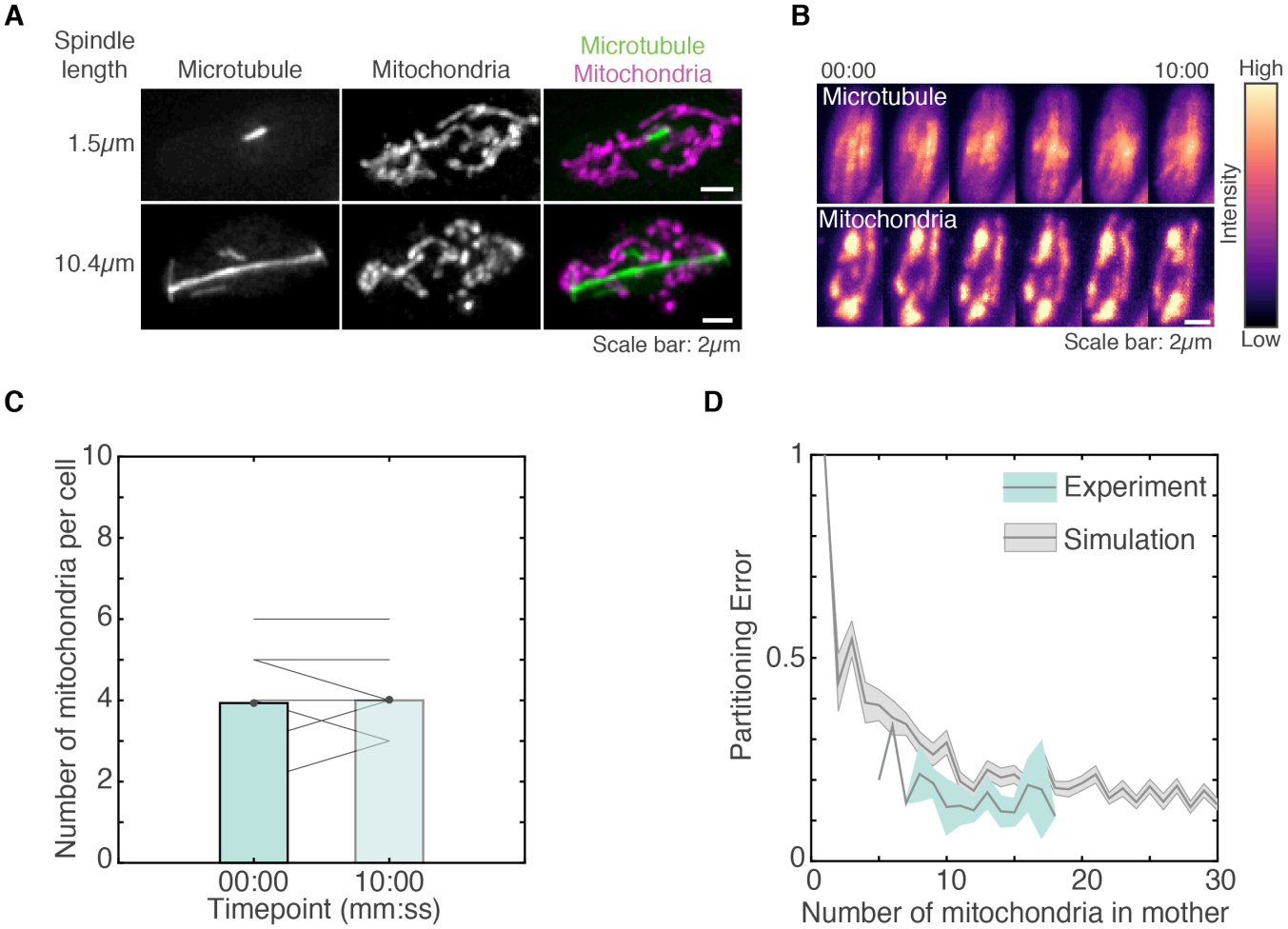

Figure S4. Mitotic spindle length does not influence number of mitochondria. **(A)** Maximum intensity projections of deconvolved Z-stack images of the microtubules (left), mitochondria (centre) and their composite (right) of WT cells (strain KI001, see Table S1) with short (top) and long (bottom) mitotic spindles. The length of the spindle is indicated to the left of the images. **(B)** Montage of maximum intensity projected confocal Z-stack images of the microtubules (top) and mitochondria (bottom) in a non-mitotic wild-type cell (strain KI001, see Table S1) represented in the intensity map indicated to the right of the images. **(C)** Bar plot of the mean number of mitochondria per cell before ('00:00') and after ('10:00') the same time window for which mitotic cells were monitored in Fig. 3C, d. Solid grey lines represent data from individual cells (n=7 cells). **(D)** Plot of number of mitochondria in mother cell vs. partitioning error (see Supplementary Information) between daughter cells in simulation (grey) and experiments (blue) expressed as mean (solid grey line) and standard error of the mean (shaded area).

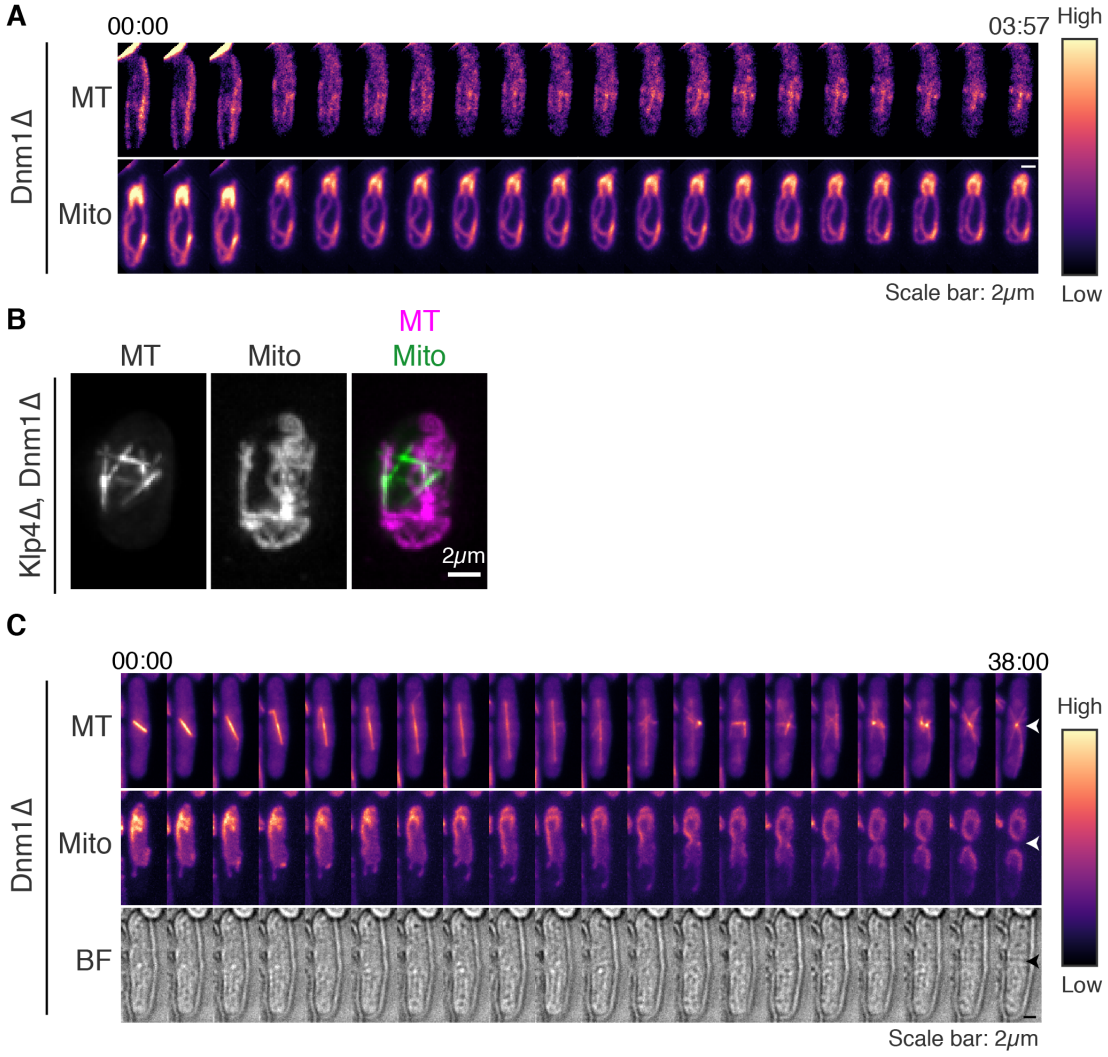

Figure S5. Mitochondrial fission requires Dnm1. (A) Montage of maximum intensity projected confocal Z-stack images of the microtubules ('MT', top) and mitochondria ('Mito', bottom) in a Dnm1Δ cell transformed with plasmid FYP2026 (see Table S1) treated with MBC. '00:00' indicates time 2min after addition of MBC (50μg/ml). **(B)** Maximum intensity projections of deconvolved Z-stack images of the microtubules (left), mitochondria (centre) and their composite (right) of Klp4Δ, Dnm1Δ cells (strain VA084, see Table S1). **(C)** Montage of maximum intensity projected confocal Z-stack images of the microtubules ('MT', top), mitochondria ('Mito', center) and bright-field channel ('BF', bottom) in a Dnm1Δ cell undergoing cell division. The location of the septum is indicated with the white and black arrowheads. The intensity map is indicated to the right of the images. Time is indicated above the images in mm:ss.

A

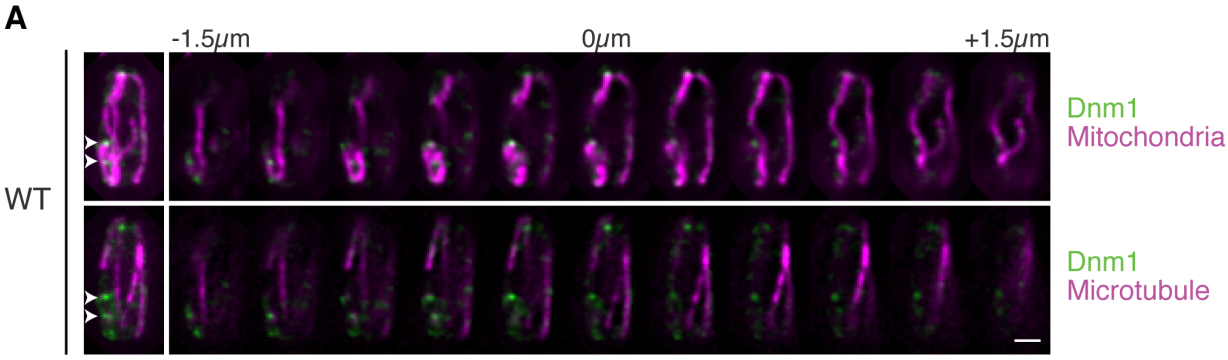

B

Parameter	Value (mean ± s.e.m)		
	WT	MT_{long}	MT_{short}
Number of mitochondria	4.9 ± 0.4	2.3 ± 0.4	10 ± 0.9
Normalized total volume of mitochondria	1.00 ± 0.10	1.09 ± 0.13	0.92 ± 0.07
Normalized volume of individual mitochondria	1.00 ± 0.16	2.30 ± 0.50	0.45 ± 0.04
Size of mitochondria (μm)	2.72 ± 0.03	6.53 ± 0.11	1.77 ± 0.02
Size of mitochondria normalized to cell length	0.35 ± 0.01	0.59 ± 0.01	0.23 ± 0.01
Circularity of mitochondria	0.60 ± 0.01	0.44 ± 0.01	0.71 ± 0.01
Aspect ratio of mitochondria	2.84 ± 0.04	3.55 ± 0.07	2.16 ± 0.03
Mitochondrial fission frequency (s^{-1})	0.018 ± 0.002	0.006 ± 0.001	0.032 ± 0.005
Mitochondrial fusion frequency (s^{-1})	0.017 ± 0.002	0.011 ± 0.001	0.025 ± 0.005

Figure S6: Measurement of mitochondrial dynamics. (A) Maximum intensity projections of deconvolved composite Z-stack images of Dnm1 and mitochondria (green and magenta respectively, top left) and Dnm1 and microtubules (green and magenta respectively, bottom left) in a wild-type cell expressing fluorescent Dnm1 and tubulin (strain MTY271 transformed with pREP41-Dnm1-Cterm-GFP, see Table S1), and stained with Mitotracker Deep Red. A majority of Dnm1 spots did not localize to mitochondria bound to the microtubule, but localize on the mitochondria away from the microtubule (white arrowheads). A montage of each 0.3μm z-slice is represented to the right of the maximum intensity projected images. The distance from the central slice ('0μm') is indicated above the montage. Scale bar represents 2μm. **(B)** Measured parameters relating to mitochondrial numbers and morphology in WT, MT_{long} and MT_{short} interphase cells represented as mean ± s.e.m.

807 **Supplementary files**

808 **Movie S1.** Live-cell confocal microscopy of MBC-treated interphase fission yeast
809 cells with the mitochondria stained with Mitotracker. Warmer colours indicate higher
810 intensities. Images were acquired at 2min intervals. Time 00:00 (mm:ss) indicates
811 time of addition of MBC. Imaging was resumed 15min after MBC addition ('15:00').
812 Scale bar represents 2μm. This movie corresponds to Fig. S1C.

813 **Movie S2.** 3D projection of microtubules (green) and mitochondria (magenta) in a
814 wild-type cell (strain KI001, see Table S1). This movie corresponds to Fig. 1A.

815 **Movie S3.** 3D projection of microtubules (green) and mitochondria (magenta, stained
816 with Mitotracker) in a Klp5Δ/Klp6Δ cell (strain G3B, see Table S1). This movie
817 corresponds to Fig. 1A.

818 **Movie S4.** 3D projection of microtubules (green) and mitochondria (magenta, stained
819 with Mitotracker) in a Klp4Δ cell (strain G5B, see Table S1). This movie corresponds
820 to Fig. 1A.

821 **Movie S5.** Mitochondrial dynamics in a wild-type cell (strain KI001, see Table S1)
822 stained with Mitotracker. A 5-slice Z-stack with step size of 0.5μm was obtained
823 every 12s. The movie represents the maximum-intensity projected images of the
824 stacks obtained. Warmer colours indicate higher intensity. The closed white
825 arrowhead points to a fusion event and the open white arrowhead points to a fission
826 event. Scale bar represents 2μm. This movie corresponds to Fig. 2A.

827 **Movie S6.** Mitochondrial dynamics in a Klp5Δ/Klp6Δ cell (strain G3B, see Table S1)
828 stained with Mitotracker. A 5-slice Z-stack with step size of 0.5μm was obtained
829 every 12s. The movie represents the maximum-intensity projected images of the
830 stacks obtained. Warmer colours indicate higher intensity. The closed white

831 arrowhead points to a fusion event. Scale bar represents 2μm. This movie
832 corresponds to Fig. 2A.
833 **Movie S7.** Mitochondrial dynamics in a Klp4Δ cell (strain G5B, see Table S1) stained
834 with Mitotracker. A 5-slice Z-stack with step size of 0.5μm was obtained every 12s.
835 The movie represents the maximum-intensity projected images of the stacks
836 obtained. Warmer colours indicate higher intensity. The open white arrowhead points
837 to a fission event. Scale bar represents 2μm. This movie corresponds to Fig. 2A.
838 **Movie S8.** Mitochondrial dynamics in a wild-type cell treated with MBC (strain KI001,
839 see Table S1) stained with Mitotracker. A 5-slice Z-stack with step size of 0.5μm was
840 obtained every 12s. The movie represents the maximum-intensity projected images
841 of the stacks obtained. Warmer colours indicate higher intensity. The open white
842 arrowhead points to a fission event. Scale bar represents 2μm. This movie
843 corresponds to Fig. 3A.
844 **Movie S9.** Mitochondrial dynamics in a Klp5Δ/Klp6Δ cell treated with MBC (strain
845 G3B, see Table S1) stained with Mitotracker. A 5-slice Z-stack with step size of
846 0.5μm was obtained every 12s. The movie represents the maximum-intensity
847 projected images of the stacks obtained. Warmer colours indicate higher intensity.
848 The closed white arrowhead points to a fusion event. Scale bar represents 2μm. This
849 movie corresponds to Fig. 3A.
850 **Movie S10.** 3D projection of microtubules (green) and mitochondria (magenta) in a
851 wild-type mitotic cell (strain KI001, see Table S1). This movie corresponds to Fig.
852 4A.
853 **Movie S11.** Microtubule dynamics (left) and mitochondrial dynamics (right) in a wild-
854 type cell (KI001, see Table S1) at the onset of mitosis. A 5-slice Z-stack with step
855 size of 0.5μm was obtained every 2min. The movie represents the maximum-

856 intensity projected images of the stacks obtained. Warmer colours indicate higher
857 intensity. Scale bar represents 2μm. The open white arrowheads point to fission
858 events. This movie corresponds to Fig. 4B.
859 **Movie S12.** 3D projection of microtubules (green) and mitochondria (magenta) in an
860 Mmb1 Δ cell (strain PT2244, see Table S1). This movie corresponds to Fig. 6A.
861 **Movie S13.** 3D projection of microtubules (green) and mitochondria (magenta) in an
862 Klp5Δ/Klp6Δ -Mmb1 Δ cell (strain VA076, see Table S1). This movie corresponds to
863 Fig. 6A.
864